Comput Mech (2015) 56:653–676
DOI 10.1007/s00466-015-1193-7

ORIGINAL PAPER

Characterization of time-varying macroscopic electro-chemo-mechanical behavior of SOFC subjected to Ni-sintering in cermet microstructures

M. Muramatsu[1] · K. Terada[2] · T. Kawada[1] · K. Yashiro[1] · K. Takahashi[3] · S. Takase[3]

Received: 13 January 2015 / Accepted: 28 July 2015 / Published online: 15 August 2015

Abstract In order to perform stress analyses of a solid oxide fuel cell (SOFC) under operation, we propose a characterization method of its time-varying macroscopic electro-chemo-mechanical behavior of electrodes by considering the time-varying geometries of anode microstructures due to Ni-sintering. The phase-field method is employed to simulate the micro-scale morphology change with time, from which the time-variation of the amount of triple-phase boundaries is directly predicted. Then, to evaluate the time-variation of the macroscopic oxygen ionic and electronic conductivities and the inelastic properties of the anode electrode, numerical material tests based on the homogenization method are conducted for each state of sintered microstructures. In these homogenization analyses, we also have to consider the dependencies of the properties of constituent materials on the temperature and/or the oxygen potential that is supposed to change within an operation period. To predict the oxygen potential distribution in an overall SOFC structure under long-period operation, which determines reduction-induced expansive/contractive deformation of oxide materials, an unsteady problem of macroscopic oxygen ionic and electronic conductions is solved. Using the calculated stress-free strains and the homogenized mechanical properties, both of which depend on the operational environment, we carry out the macroscopic stress analysis of the SOFC.

Keywords Solid oxide fuel cell (SOFC) · Electrochemical potential · Sintering of Ni · Phase-field method · Homogenization method

✉ M. Muramatsu
muramatsu@ee.mech.tohoku.ac.jp

[1] Graduate School of Environmental Studies, Tohoku University, Aza-Aoba 6-6-01, Aramaki, Aoba-ku, Sendai 980-8579, Japan

[2] International Research Institute of Disaster Science, Tohoku University, Aza-Aoba 468-1, Aramaki, Aoba-ku, Sendai 980-0845, Japan

[3] Department of Civil Engineering, Tohoku University, Aza-Aoba 6-6, Aramaki, Aoba-ku, Sendai 980-8579, Japan

1 Introduction

Solid oxide fuel cell (SOFC) is one of the electric generating systems that attract most attention due to its cleanness and applicability to distributed power generation systems [1,2]. Figure 1 is a schematic illustration of general SOFC design. Porous oxides, which are commonly ceramic materials, are chosen for the cathode at one end, whereas cermets composed of Ni and oxide ceramic materials are used for the anode at the other end. The electrolyte made of dense ceramics is sandwiched between these two electrodes. Such a unit is called 'cell'. Generally, more than one cell are stacked together to form a cell stack of SOFC to generate high electric power. A component to connect adjacent cells in series is called an interconnect.

Since the components of SOFCs are always exposed to high temperature and large pressures of various gasses, the overall electrical performance is degraded during long-period operation with start-and-stop control. Such performance degradations are associated mainly with the aged deteriorations of physical properties of the constituent materials, which are induced by various factors [3–5]. Among them, the mechanical and thermodynamical effects come within the scope of this paper.

The mechanical effect arises mainly from the stress-free, expansive/contractive strains due to the time variations of

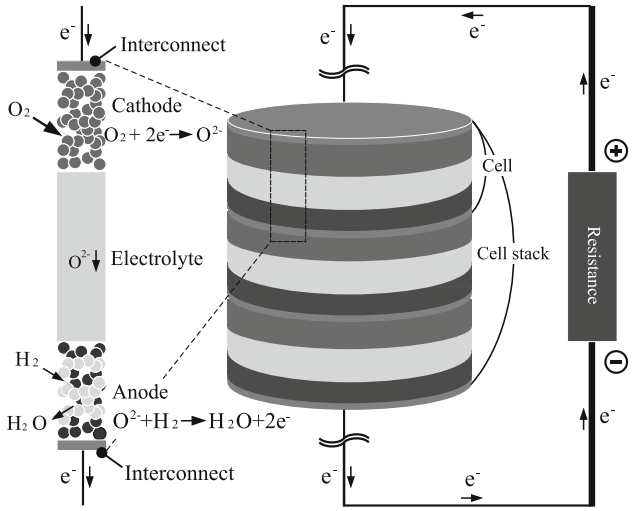

Fig. 1 System of SOFC: cell and cell stack

- operating temperature, which causes thermal deformation [6,7]
- reduction atmosphere, which causes reduction-induced deformation of ceramics materials due to non-stoichiometry [8,9], and
- reaction atmosphere, which causes oxidation-reduction (RedOx) cycling-induced deformation of Ni and NiO.

The overall deformation of a cell and its components involving these strains with different sources may cause cracks at various spatial scales, which are possibly sources of not only electrical, but also mechanical deteriorations that lead to the mechanical failure at their worst.

On the other hand, the thermodynamical effect induces the deteriorations of electrical and electrochemical performances of SOFCs' components that arise from the composition change due to poisoning and the morphological change due to sintering of Ni particles at micro-scale (or particle-size level) . In particular, notable among them is the coarsening of Ni particles in anode microstructures under operating temperature, which is lower than its melting temperature of 1453 K [10], but is close to its welding temperature from 734 to 1070 K [11]. The morphological change of anode microstructures with time due to the Ni-sintering causes not only the aged deterioration of electrical properties such as electric conductivities, but also the time-variation of mechanical characteristics of SOFC's components and materials [11,12].

A number of computational investigations have been conducted to clarify the mechanisms of such electrical and mechanical degradations in SOFCs at various spatial scales [13–17]. Oxygen potentials are calculated to predict the electric performance [18–20] and to evaluate the stress distributions of SOFC's components [21]. Several articles have been devoted to the study on the deterioration of mechanical properties during stop-and-start operations [22,23]. Recent years has seen a renewal of interest in phase-field simulations to reproduce Ni-sintering process that involves expansion and aggregation of Ni particles during the formation of anode microstructures [10,24–29].

Although these individual subjects of study on the electrical performance deterioration associated with the aforementioned thermodynamical and mechanical effects have been explored to some extent, little attention has been given to their coupling phenomena. In fact, the SOFC operations involve various types of physical phenomena at various spatial and time scales and hence their coupling behavior determines the performance of SOFS as an electrical device. Whereas overall gas flows, heat conductions, oxygen potential change and deformations are coupled at macro-scale, the corresponding macroscopic physical properties are determined by the micro-scale morphology changes with time and constituents' material properties of electrodes and of interfaces with electrolytes, which depend on temperature and oxygen potential changes. To make the prediction of performance deteriorations more reliable, such coupling phenomena have to be taken into account in our numerical simulations. In particular, it is important to notice that the morphological change of cement microstructures due to Ni-sintering conduces the time-variations of both macroscopic electrical and mechanical properties of anode components. Therefore, the characterization of this kind of time-varying, two-scale coupling behavior can be the first step to realize reliable numerical simulations to evaluate the coupled electrical and mechanical behavior of an overall cell structure.

In this context, we propose a characterization method of its time-varying macroscopic electro-chemo-mechanical behavior of electrodes by considering the time-varying geometries of anode microstructures due to Ni-sintering in order to predict the oxygen potential and stress distributions in SOFC under operations. The framework of the analysis is shown in Fig. 2. The phase-field method is employed to simulate the micro-scale morphology change of anode microstructures with time, from which we evaluate the time-variation of the amount of triple-phase boundaries, at which electrochemical reactions occur. Then, to evaluate the time-variation of the macroscopic oxygen ionic and electronic conductivities, and the inelastic properties of the anode electrode, we conduct a series of numerical material tests (NMTs) based on the homogenization method for each state of the sintered microstructures with the help of the finite element method (FEM). In these computational homogenization analyses, we take into account the dependencies of the properties of constituent materials on the temperature and/or the oxygen potential that are supposed to change within an operation period.

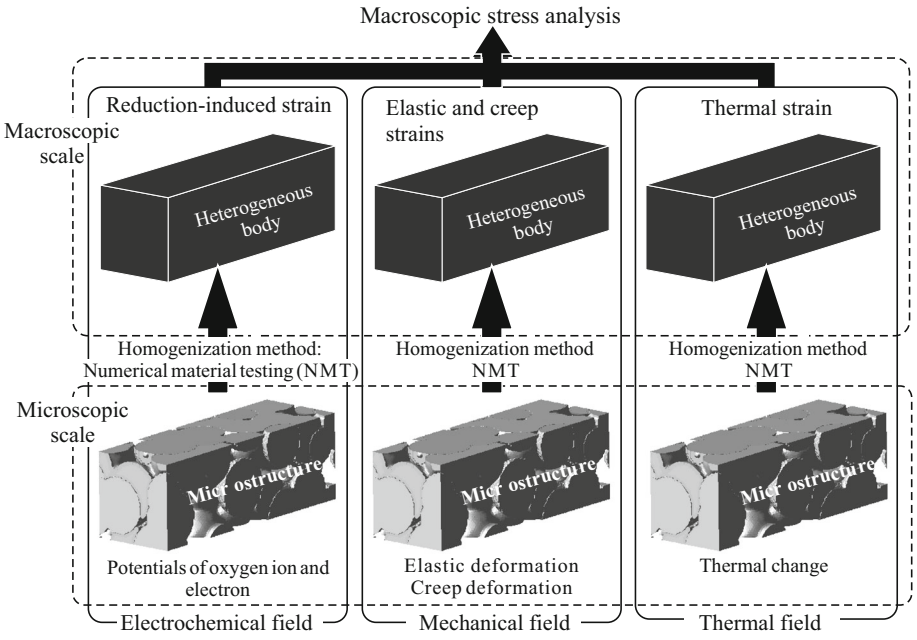

Fig. 2 Framework of analysis

With the macroscopic properties at hand that reflect the operating environment and the time-varying micro-scale morphology, we solve an unsteady coupling problem between macroscopic oxygen ionic and electronic conductions by the FEM to obtain the oxygen potential distribution in an overall cell structure under long-period operation. Then, according to the values of the oxygen potential, the amount of reduction-induced expansive/contractive strain of oxide materials can be determined. Using thus obtained information about the stress-free strains and the homogenized mechanical properties calculated in the NMTs, both of which depend on the operational environment, we carry out the macroscopic stress analysis of the SOFC to predict the overall deformation and to examine the possibilities of mechanical damage during the start-and-stop operation.

The novel contribution of this paper is the development of the framework to reproduce the complicated mechanical behavior of SOFC under operational environment, which possibly induces electrochemical and mechanical deteriorations. During the process of the development, we introduced an idea of applying computational homogenization method to characterize the time-varying degradation phenomena of the macroscopic electrochemical and mechanical properties by the corresponding microscopic analyses. This study computationally contributes to the development of the numerical homogenization method of the electrochemical potential equations.

2 Framework of two-scale analysis

2.1 Electrochemical reactions in SOFC

At the cathode electrode, oxygen O_2 is reduced by electron e^- to produce oxygen ion O^{2-}, which can move through the electrolyte toward the anode electrode. The oxygen ion that reaches the anode electrode is oxidized by the reaction with H_2, which is provided as a fuel, to produce water H_2O and e^-. These electro-chemical reactions are respectively written as

$$\text{Cathode:}\quad \frac{1}{2}O_2 + 2e^- \rightarrow O^{2-} \tag{1}$$

$$\text{Anode:}\quad O^{2-} + H_2 = H_2O + 2e^- \tag{2}$$

Since the electrodes are porous materials, actual reactions are expected to occur at the interfaces between gas and solid phases. The latter electro-chemical reaction, i.e., oxidation with emission of electrons, occurs at the so-called triple phase boundaries (TPBs) of the anode electrode, which is generally a cermet composed of Ni particles and ion conductive ceramics. On the other hand, the cathode electrode, whose constituents are mixed ionic–electronic conductive ceramics, allows the reduction of O_2 at the so-called dual phase boundaries (DPBs) [11], involving the ionization of the oxygen with absorption of electrons.

The electronic current density $i_{e^-}^{\text{Anode}}$ generated with the oxidation (2) is known to be determined by the Butler–Volmer relationship [2,30] as

$$i_{e^-}^{\text{Anode}} = i_0^{\text{Anode}} \left\{ \exp\left(\frac{2\alpha_a F}{R\theta} \Delta E \right) - \exp\left(-\frac{2\alpha_c F}{R\theta} \Delta E \right) \right\} \tag{3}$$

where $F = 96,500\ \text{C mol}^{-1}$ is the Faraday's constant, R is the gas constant, θ is the microscopic temperature, and i_0^{Anode} is the exchange current density. Also, α_a and α_c are respectively the anodic and cathodic charge transfer coefficients and ΔE is the polarization voltage evaluated by

$$\Delta E = \frac{\mu_O - \mu_O^g}{2F} \tag{4}$$

where μ_O and μ_O^g are the oxygen potentials in the anode materials and in the gas phase, respectively. The oxygen potential μ_O is calculated with the partial pressure of oxygen p_{O_2} as

$$\mu_O = \mu_O^\circ + \frac{1}{2} R\theta \ln p_{O_2} \tag{5}$$

where the oxygen potential at standard condition μ_O° is set as zero. Then, the normal component of current density $\boldsymbol{i}_{e^-}$ inside the Ni particles must be equal to the generated electronic current density as

$$i_{e^-} = \boldsymbol{i}_{e^-} \cdot \boldsymbol{n} = i_{e^-}^{\text{Anode}} \tag{6}$$

where $\boldsymbol{n}$ is the outward unit vector on the TPB, directed to the normal to the Ni surfaces.

A TPB is generally identified as a line shared by three phases, e.g, gas, Ni and YSZ phases. However, since boundary conditions must be imposed on surfaces, it is assumed in this study that the boundary on which the electrochemical reaction produces electrons or ions a small and adjacent surface region around the line of the TPB and that the electronic current is associated with the normal direction to the surface region of Ni. On the other hand, the ionic current assumed to be consumed on a small surface region adjacent to the TPB line.

According to the electro-chemical reaction (2), the oxygen ionic current density generated at the same boundary surfaces can be evaluated as

$$i_{O^{2-}} = \boldsymbol{i}_{O^{2-}} \cdot \boldsymbol{n}' = i_{O^{2-}}^{\text{Anode}} = -i_{e^-}^{\text{Anode}} \tag{7}$$

where the outward unit vector $\boldsymbol{n}'$ is defined on the TPB, directed to the normal to the oxide's surfaces.

The current density generated at the cathode with the reduction process (1) can also be determined by the Butler–Volmer type equation as

$$i_{e^-}^{\text{Cathode}} = i_0^{\text{Cathode}} \left\{ \exp\left(\frac{2\alpha_a F}{R\theta} \Delta E \right) - \exp\left(-\frac{2\alpha_c F}{R\theta} \Delta E \right) \right\} \tag{8}$$

where the exchange current density i_0^{Cathode} and the charge transfer coefficients are different from those for the anode. The relationships of this generated current density with the normal components of the current densities inside the oxide are given as

$$i_{e^-} = \boldsymbol{i}_{e^-} \cdot \boldsymbol{n} = i_{e^-}^{\text{Cathode}} \tag{9}$$

$$i_{O^{2-}} = \boldsymbol{i}_{O^{2-}} \cdot \boldsymbol{n}' = i_{O^{2-}}^{\text{Cathode}} = -i_{e^-}^{\text{Cathode}} \tag{10}$$

The boundary conditions given to TPBs and DPBs at micro-scale are presented in (6), (7), (9) and (10). Each of these is a special type of transfer boundary conditions, since the amount of current generated or consumed at TPBs and DPs is governed by the so-called Butler–Volmer relationship (8), which is excited by the difference between potentials in solid (Ni or YSZ) and gas phases. In other words, the currents flowing in and out are calculated with (8) with the partial pressures of oxygen in the gas and solid phases, and the calculated currents are given to the boundaries in this study.

2.2 Two-scale modeling strategy

Although the electro-chemical reactions described above occur at micro-scale, our main concern is the characterization of the coupling behavior between the overall electrical conduction with electro-chemical reactions and deformations at a spatial scale of a cell or stack level. The schematic illustration shown in Fig. 3 represents the idea of our two-scale modeling in this study. Since the porous microstructures of the electrodes are too small to analyze directly, they are replaced by the equivalent homogeneous media to describe and analyze the overall behavior of SOFC's cells. In this context, we apply the idea of mathematical homogenization [31,32] to derive the two-scale boundary value problems for electric conductions with electrochemical reactions and deformations.

As can be seen later, the electrical conduction and deformation problems to be solved are almost standard. One of the non-standard phenomena in our two-scale molding based on the homogenization method could be the boundary conditions (BCs) associated with the above-described electrochemical reactions on pore surfaces in the electric

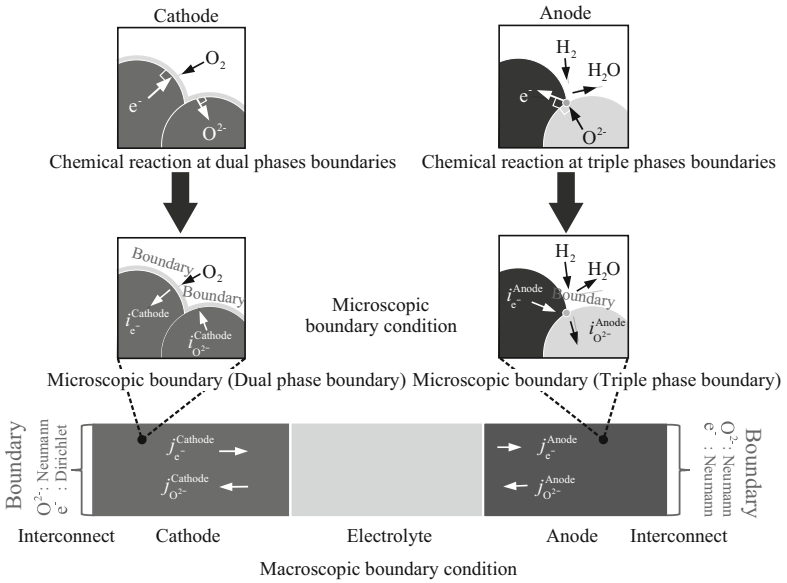

Fig. 3 Two-scale modeling of SOFC

condition problems. That is, while the microscopic electrical conduction problems involve a sort of transfer BCs on the TPB and DPB surfaces, the macroscopic or homogenized electrodes no longer have pores. However, a similar phenomena can be found in the heat conduction problems in porous media with micro-scale heat transfer and the corresponding two-scale model based on the homogenization has already been proposed in [33], whose formulation can be diverted to the present electrical conduction problems in SOFCs.

Also, we are concerned with the time-variation of the anode microstructures due to Ni-sintering. That is, the microstructures that determine the macroscopic electrical condition with electrochemical reactions and deformation characteristics change in time. To capture the micro-scale geometrical changes in time, we employ the phase-field method, which is suitable for the representation of the morphological change due to solid-state diffusion. Then, the homogenization method can be applied to some selected states of the sintered anode microstructures to characterize the time-varying macroscopic material properties. However, it is assumed that the unsteady effects at micro-scale can be negligible so that the first-order homogenization, which neglects the actual spatial sizes of microstructures, is applicable. This assumption for the two-scale modeling would be possible, if the micro-scale unsteady conduction phenomena is very fast compared with the corresponding macroscopic ones; see [33].

3 Formulation

3.1 Microscopic electronic and oxygen-ionic conduction problems

The electrical conduction in mixed ionic–electronic conductive ceramics can be characterized by the local transport of electro-chemical potentials and is governed by the following equations:

$$\mu_{\mathrm{O}} = \eta_{\mathrm{O}^{2-}} - 2\eta_{\mathrm{e}^-} \tag{11}$$

$$\frac{c}{-2F}\dot{\mu}_{\mathrm{O}} = -\nabla \cdot \boldsymbol{i}_{\mathrm{O}^{2-}} \tag{12}$$

$$\frac{c}{-2F}(-\dot{\mu}_{\mathrm{O}}) = -\nabla \cdot \boldsymbol{i}_{\mathrm{e}^-} \tag{13}$$

$$c(\mu_{\mathrm{O}}) = -\frac{4F^2}{V_{\mathrm{m}}}\frac{\partial \delta(\mu_{\mathrm{O}})}{\partial \mu_{\mathrm{O}}} \tag{14}$$

$$\boldsymbol{i}_{\mathrm{O}^{2-}} = -\left(\frac{\sigma_{\mathrm{O}^{2-}}}{-2F}\right)\nabla \eta_{\mathrm{O}^{2-}} \tag{15}$$

$$\boldsymbol{i}_{\mathrm{e}^-} = -\left(\frac{\sigma_{\mathrm{e}^-}}{-2F}\right)\nabla (2\eta_{\mathrm{e}^-}) \tag{16}$$

$$\boldsymbol{i} = \boldsymbol{i}_{\mathrm{e}^-} + \boldsymbol{i}_{\mathrm{O}^{2-}} \tag{17}$$

where the field variables and material properties are defined as follows:

μ_{O} : oxygen potential
$\eta_{\mathrm{O}^{2-}}$: electro-chemical potential of oxygen ion
η_{e^-} : electro-chemical potential of electron
$\boldsymbol{i}$: total current density
$\boldsymbol{i}_{\mathrm{e}^-}$: electronic current density
$\boldsymbol{i}_{\mathrm{O}^{2-}}$: oxygen-ionic current
$j_{\mathrm{O}^{2-}} = -j_{\mathrm{e}^-}$: reaction current density at electrodes
$\sigma_{\mathrm{O}^{2-}}$: oxygen ionic conductivity
σ_{e^-} : electronic conductivity
c : electric capacitance
V_{m} : molal volume
δ : oxygen non-stroiciometry or vacancy

It is noted that the source terms are not included in (12) and (13). Instead, the reaction currents are generated on the DPBs and TPBs as described in the previous section; see (6), (7), (9) and (10). With these BCs on the pore surfaces at micro-scale, we have the standard Dirchiclet BC, for which the values of the electro-chemical potentials are prescribed as

$$\eta_{\mathrm{O}^{2-}} = \bar{\eta}_{\mathrm{O}^{2-}} \quad \text{on} \quad \Gamma_{\eta_{\mathrm{O}^{2-}}} \tag{18}$$

$$\eta_{\mathrm{e}^-} = \bar{\eta}_{\mathrm{e}^-} \quad \text{on} \quad \Gamma_{\eta_{\mathrm{e}^-}} \tag{19}$$

where $\bar{\bullet}$ indicates prescribed values. Also, the amounts of external electronic and oxygen-ionic current densities can be prescribed on the Neumann boundaries as

$$i_{\mathrm{O}^{2-}} = \boldsymbol{i}_{\mathrm{O}^{2-}} \cdot \boldsymbol{n} = \bar{i}_{\mathrm{O}^{2-}} \quad \text{on} \quad \Gamma_{i_{\mathrm{O}^{2-}}} \tag{20}$$

$$i_{\mathrm{e}^-} = \boldsymbol{i}_{\mathrm{e}^-} \cdot \boldsymbol{n} = \bar{i}_{\mathrm{e}^-} \quad \text{on} \quad \Gamma_{i_{\mathrm{e}^-}} \tag{21}$$

The substitution of (11), (15) and (16) into (12) and (13) yields the following evolution equations:

$$\frac{c}{-2F}\left(\dot{\eta}_{\mathrm{O}^{2-}} - 2\dot{\eta}_{\mathrm{e}^-}\right) = -\nabla \cdot \left\{ -\left(\frac{\sigma_{\mathrm{O}^{2-}}}{-2F}\right) \nabla \eta_{\mathrm{O}^{2-}} \right\} \tag{22}$$

$$\frac{c}{-2F}\left(2\dot{\eta}_{\mathrm{e}^-} - \dot{\eta}_{\mathrm{O}^{2-}}\right) = -\nabla \cdot \left\{ -\left(\frac{\sigma_{\mathrm{e}^-}}{-2F}\right) \nabla \left(2\eta_{\mathrm{e}^-}\right) \right\} \tag{23}$$

Once the solutions of these equations, $\eta_{\mathrm{O}^{2-}}$ and η_{e^-}, are obtained, the oxygen potential can be evaluated with (11).

Here, (22) and (23) are tightly coupled and solved for both of the electrochemical potentials simultaneously.

3.2 Microscopic deformation problem

Some sorts of metallic oxides used for components of SOFC exhibit the so-called oxygen non-stoichiometry. To be more specific, the vacancies are generated in the materials due to the release of oxygen ions into the air to meet the balance of the oxygen potentials between gas and solid phases, when metallic oxides are subjected to a reductive atmosphere resulted from the decrease in oxygen partial pressure. The resulting electrically non-equilibrated state invokes the expansion of the material. This expansive deformation is stress-free, just like thermal expansions, and is called the reduction-induced (chemical) expansion.

Considering both the thermal and reduction-induced strains, we define the microscopic deformation problem by the following governing equations:

$$\nabla \cdot \boldsymbol{\sigma} + \rho \boldsymbol{b} = \boldsymbol{0} \tag{24}$$

$$\boldsymbol{\varepsilon} = \boldsymbol{\varepsilon}^{\mathrm{e}} + \boldsymbol{\varepsilon}^{\mathrm{c}} + \boldsymbol{\varepsilon}^{\theta} + \boldsymbol{\varepsilon}^{\mathrm{r}} \tag{25}$$

$$\boldsymbol{\sigma} = \mathbb{C} : \boldsymbol{\varepsilon}^{\mathrm{e}} = \kappa \varepsilon_{\mathrm{v}}^{\mathrm{e}} \boldsymbol{1} + 2\mu \boldsymbol{e}^{\mathrm{e}} \tag{26}$$

$$\dot{\boldsymbol{\varepsilon}}^{\mathrm{c}} = \dot{\gamma} \frac{\boldsymbol{s}}{||\boldsymbol{s}||} \tag{27}$$

$$\dot{\gamma} = C_1 |\bar{\sigma}|^{C_2} \exp\left(-\frac{C_3}{\theta}\right) \tag{28}$$

$$\boldsymbol{\varepsilon}^{\theta} = \Delta\theta \alpha^{\theta} \boldsymbol{1} \tag{29}$$

$$\boldsymbol{\varepsilon}^{\mathrm{r}} = \Delta\delta \beta^{\mathrm{r}} \boldsymbol{1} \tag{30}$$

along with the Dirichlet and Neumann conditions on the boundaries Γ_u and Γ_t, respectively given as

$$\boldsymbol{u} = \bar{\boldsymbol{u}} \quad \text{on} \quad \Gamma_u \tag{31}$$

$$\boldsymbol{t} = \boldsymbol{\sigma}\boldsymbol{n} = \bar{\boldsymbol{t}} \quad \text{on} \quad \Gamma_t \tag{32}$$

Here, the field variables and material parameters are defined as follows:

$\boldsymbol{\sigma}$: Cauchy stress tensor
$\boldsymbol{s}$: deviatoric stress tensor
$\bar{\sigma}$: von-Mises equivalent stress
ρ : mass density
$\boldsymbol{b}$: body force vector
$\boldsymbol{u}$: displacement vector
$\boldsymbol{\varepsilon}$: total strain tensor
$\boldsymbol{\varepsilon}^{\mathrm{e}}$: elastic strain tensor
$\boldsymbol{\varepsilon}^{\mathrm{c}}$: creep strain tensor
$\boldsymbol{\varepsilon}^{\theta}$: thermal strain tensor
$\boldsymbol{\varepsilon}^{\mathrm{r}}$: reduction-induced strain tensor
$\boldsymbol{e}^{\mathrm{e}}$: deviatoric part of elastic strain
$\varepsilon_{\mathrm{v}}^{\mathrm{e}} = \varepsilon_{pp}^{\mathrm{e}}$: volumetric component of elastic strain
$\bar{\boldsymbol{u}}$: specified displacement vector
$\boldsymbol{t}$: traction vector on boundary surfaces
$\bar{\boldsymbol{t}}$: external surface force vector
$\mathbb{C}$: fourth-order elasticity tensor
κ : bulk modulus of elasticity
μ : shear modulus of elasticity
$\dot{\gamma}$: creep multiplier
$||\boldsymbol{s}|| = \sqrt{s_{ij}s_{ij}}$: norm of deviatoric stress $\boldsymbol{s}$
$C_1,\ C_2,\ C_3$: creep material parameters

α^{θ} : coefficient of thermal expansion
β^{r} : coefficient of reduction-induced expansion
$\Delta\theta$: change in temperature
$\Delta\delta$: change in vacancy

3.3 Homogenization

The standard formulation in the mathematical homogenization theory starts with the introduction of micro- and macroscopic domains along with their own coordinate systems. In particular, the domain of the microscopic problems, usually denoted by Y, is recognized as that of a representative volume element (RVE) with geometrical periodicity, which is often referred to as unit cell. Also, microscopic coordinate $\boldsymbol{y}$ is introduced to measure the electro-chemo-mechanical behavior at micro-scale. Thus, in order to characterize the macroscopic material parameters by the homogenization method, we just re-define the governing equations provided in the previous section in Y with microscopic coordinate $\boldsymbol{y}$.

For linear material models, the resulting homogenized material properties can be calculated by the following formulae with the pre-determined characteristic functions ζ_{I}^{k}, $\boldsymbol{\chi}^{kh}$, ψ_{θ} and ψ_{δ} ($k = 1, 2, 3, h = 1, 2, 3$; see for example [33]):

$$\tilde{\boldsymbol{\sigma}}_{\mathrm{I}} = \frac{1}{|Y|}\int_{Y} \boldsymbol{\sigma}_{\mathrm{I}} \cdot \left(\mathbf{1}^{k} - \nabla_{y}\zeta_{\mathrm{I}}^{k}\right)\mathrm{d}y \tag{33}$$

$$\tilde{\mathbb{C}} = \frac{1}{|Y|}\int_{Y} \mathbb{C} : \left(\mathbf{I}^{kh} - \nabla_{y}\boldsymbol{\chi}^{kh}\right)\mathrm{d}y \tag{34}$$

$$\tilde{\boldsymbol{\alpha}} = \tilde{\mathbb{C}}^{-1} : \left(\frac{1}{|Y|}\int_{Y} \mathbb{C} : \left(\boldsymbol{\alpha} - \nabla_{y}\psi_{\theta}\right)\mathrm{d}y\right) \tag{35}$$

$$\tilde{\boldsymbol{\beta}} = \tilde{\mathbb{C}}^{-1} : \left(\frac{1}{|Y|}\int_{Y} \mathbb{C} : \left(\boldsymbol{\beta} - \nabla_{y}\psi_{\delta}\right)\mathrm{d}y\right) \tag{36}$$

where $|Y|$ is the volume of unit cell, $\tilde{\sigma}_{\mathrm{I}}$ ($\mathrm{I} = \mathrm{O}^{2-}$ and e^{-}) are the electronic and ionic conductivities, $\tilde{\mathbb{C}}$ is the homogenized elasticity tensor, $\tilde{\boldsymbol{\alpha}}$ is the homogenized coefficient of thermal expansion (CTE) and $\tilde{\boldsymbol{\beta}}$ is the homogenized coefficient of reduction-induced expansion (CRE) . Also, we have defined some symbols using Kronecker's delta symbol δ_{ij} such that $\mathbf{1}^{k} = \delta_{ik}\boldsymbol{e}_{i}$, $\mathbf{I}^{kh} = \delta_{ik}\delta_{jh}\boldsymbol{e}_{i} \otimes \boldsymbol{e}_{j}$, $\boldsymbol{\alpha} = \alpha^{\theta}\delta_{ij}\boldsymbol{e}_{i} \otimes \boldsymbol{e}_{j}$ and $\boldsymbol{\beta} = \beta^{\mathrm{r}}\delta_{ij}\boldsymbol{e}_{i} \otimes \boldsymbol{e}_{j}$. Here, the gradient operation with respect to micro-scale $\boldsymbol{y}$ is explicitly denoted by ∇_{y}. The characteristic functions necessary to calculate the homogenized material properties (33)–(36) can be obtained by solving the following governing equations:

$$\nabla_{y} \cdot \left(\boldsymbol{\sigma}_{\mathrm{I}} \cdot \nabla_{y}\zeta_{\mathrm{I}}^{k}\right) = \nabla_{y} \cdot \left(\boldsymbol{\sigma}_{\mathrm{I}} \cdot \mathbf{1}^{k}\right) \tag{37}$$

$$\nabla_{y} \cdot \left(\mathbb{C} : \nabla_{y}\boldsymbol{\chi}^{kh}\right) = \nabla_{y} \cdot \left(\mathbb{C} : \mathbf{I}^{kh}\right) \tag{38}$$

$$\nabla_{y} \cdot \left(\mathbb{C} : \nabla_{y}\psi_{\theta}\right) = \nabla_{y} \cdot \left(\mathbb{C} : \boldsymbol{\alpha}\right) \tag{39}$$

$$\nabla_{y} \cdot \left(\mathbb{C} : \nabla_{y}\psi_{\delta}\right) = \nabla_{y} \cdot \left(\mathbb{C} : \boldsymbol{\beta}\right) \tag{40}$$

It is to be noted that formulae (33)–(36) make sense only when the problems are linear. When the nonlinearities have to be considered, we directly solve the microscopic governing equations in Sects. 3.1 and 3.2 with definition of a periodic RVE domain and appropriate BCs to obtain the representative macroscopic stress–strain curves. This process is called the numerical material testing (NMT) [34]. Then, assuming that the functional forms of macroscopic constitutive equations can be found, we apply an optimization method to identify the material parameters with respect to the obtained macroscopic stress–strain responses. The method of nonlinear homogenization with NMT in this context is presented in references [34,35].

Also, the homogenized capacitance $\tilde{c}$ and homogenized body force $\tilde{\boldsymbol{b}}$ are respectively evaluated as

$$\tilde{c} = \frac{1}{|Y|}\int_{Y} c\,\mathrm{d}y \tag{41}$$

$$\tilde{\boldsymbol{b}} = \frac{1}{|Y|}\int_{Y} \boldsymbol{b}\,\mathrm{d}y \tag{42}$$

The macroscopic reaction current $\tilde{j}$ is expressed by using microscopic reaction area Y^{reac} and the current density in unit reaction area i^{reac}.

$$\tilde{j}_{\mathrm{K}} = \frac{1}{|Y|}\int_{\partial Y_{\mathrm{v}}} i_{\mathrm{K}}\,\mathrm{d}s \tag{43}$$

where K takes e^{-} or O^{2-}, and i_{K} is the microscopic reaction current defined in (6), (7), (9) or (10). Also, ∂Y_{v} is the surface region of the TPB or DPB so that $\frac{1}{|Y|}\int_{\partial Y_{\mathrm{v}}} \bullet \mathrm{d}s$ indicates the volume average of the surface integral of $\bullet$ for unit cells. According to the previous report [33], the reaction current in the macroscopic electronic and ionic conduction problems are used for source terms and are evaluated as

$$\tilde{j}_{\mathrm{e}^{-}}^{\mathrm{Cathode}} = A_{\mathrm{DPB}}\, i_{\mathrm{e}^{-}}^{\mathrm{Cathode}} \tag{44}$$

$$\tilde{j}_{\mathrm{e}^{-}}^{\mathrm{Anode}} = L_{\mathrm{TPB}}\, i_{\mathrm{e}^{-}}^{\mathrm{Anode}} \tag{45}$$

where A_{DPB} and L_{TPB} are the total areas of DPBs and TPBs, respectively. With these formulae and by the definitions of the microscopic reaction currents, the equality $\tilde{j}_{\mathrm{O}^{2-}}^{\mathrm{I}} = -\tilde{j}_{\mathrm{e}^{-}}^{\mathrm{I}}$ ($\mathrm{I} = \mathrm{Cathode}$ or Anode) is trivial.

3.4 Macroscopic electro-chemo-mechanics problems

The local transport of macroscopic electro-chemical potentials is governed by the following equations:

$$\tilde{\mu}_{\mathrm{O}} = \tilde{\eta}_{\mathrm{O}^{2-}} - 2\tilde{\eta}_{\mathrm{e}^-} \tag{46}$$

$$\frac{\tilde{c}}{-2F}\dot{\tilde{\mu}}_{\mathrm{O}} = -\nabla\cdot\tilde{\boldsymbol{i}}_{\mathrm{O}^{2-}} + \tilde{j}_{\mathrm{O}^{2-}} \tag{47}$$

$$\frac{\tilde{c}}{-2F}\left(-\dot{\tilde{\mu}}_{\mathrm{O}}\right) = -\nabla\cdot\tilde{\boldsymbol{i}}_{\mathrm{e}^-} + \tilde{j}_{\mathrm{e}^-} \tag{48}$$

$$\tilde{\boldsymbol{i}}_{\mathrm{O}^{2-}} = -\left(\frac{\tilde{\boldsymbol{\sigma}}^{\mathrm{i}}_{\mathrm{O}^{2-}}}{-2F}\right)\cdot\nabla\tilde{\eta}_{\mathrm{O}^{2-}} \tag{49}$$

$$\tilde{\boldsymbol{i}}_{\mathrm{e}^-} = -\left(\frac{\tilde{\boldsymbol{\sigma}}^{\mathrm{i}}_{\mathrm{e}^-}}{-2F}\right)\cdot\nabla\left(2\tilde{\eta}_{\mathrm{e}^-}\right) \tag{50}$$

$$\tilde{\boldsymbol{i}} = \tilde{\boldsymbol{i}}_{\mathrm{e}^-} + \tilde{\boldsymbol{i}}_{\mathrm{O}^{2-}} \tag{51}$$

where symbol $\tilde{\bullet}$ indicates the macroscopic (homogenized) quantity of the corresponding microscopic quantity $\bullet$. Here, the term "macro" implies "average" or "apparent" in the sense that the heterogeneities of electrodes' porous microstructures are replaced by equivalent homogeneous media (Fig. 2). The substitution of (46), (49) and (50) into (52) and (53) yields the following evolution equations:

$$\frac{\tilde{c}^{\mathrm{i}}}{-2F}\left(\dot{\tilde{\eta}}_{\mathrm{O}^{2-}} - 2\dot{\tilde{\eta}}_{\mathrm{e}^-}\right) = -\nabla\cdot\left\{-\left(\frac{\tilde{\boldsymbol{\sigma}}^{\mathrm{i}}_{\mathrm{O}^{2-}}}{-2F}\right)\cdot\nabla\tilde{\eta}_{\mathrm{O}^{2-}}\right\} + \tilde{j}_{\mathrm{O}^{2-}} \tag{52}$$

$$\frac{\tilde{c}^{\mathrm{i}}}{-2F}\left(2\dot{\tilde{\eta}}_{\mathrm{e}^-} - \dot{\tilde{\eta}}_{\mathrm{O}^{2-}}\right) = -\nabla\cdot\left\{-\left(\frac{\tilde{\boldsymbol{\sigma}}^{\mathrm{i}}_{\mathrm{e}^-}}{-2F}\right)\cdot\nabla\left(2\tilde{\eta}_{\mathrm{e}^-}\right)\right\} + \tilde{j}_{\mathrm{e}^-} \tag{53}$$

Once the solutions of these equations, $\tilde{\eta}_{\mathrm{O}^{2-}}$ and $\tilde{\eta}_{\mathrm{e}^-}$, are determined, the macroscopic oxygen potential $\tilde{\mu}_{\mathrm{O}}$ can be evaluated with (46) so that the macroscopic reduction-induced strain can be evaluated by the multiplication of macroscopic vacancy $\tilde{\delta}$ by the coefficient (36). Here, the macroscopic vacancy can be evaluated as the volume average of the microscopic vacancy, which can be taken as empirical relationships with the microscopic oxygen potential or oxygen partial pressure.

The macroscopic partial pressures of oxygen $\tilde{p}_{\mathrm{O}_2}$ and vacancy $\tilde{\delta}$ are regarded as the volume-averaged quantities of microscopic oxygen partial pressure p_{O_2} and vacancy δ over a unit cell. The relationship between p_{O_2} and δ must be determined with relevant experimental data and then $\tilde{p}_{\mathrm{O}_2}$ and $\tilde{\delta}$ can be calculated accordingly under the assumption that the latter inherits the former.

Here, (46) is the local equilibrium equation of macroscopic electrochemical potentials of oxygen ion and electron, and (52) and (53) are the evolution equations of the macroscopic potentials of oxygen ion and electron along with constitutive relations (49) and (50), and (51) is the definition of total current. These are a set of governing equations for the macroscopic conduction problem for electrochemical potentials of electron and ions. After the calculation of the characteristic functions by solving (37)–(30) for a single unit cell which can be regarded as a subdomain, this macroscopic problem governed by (46)–(51) is solved. Thus, the calculations for the unit cell and the macrostructure are carried out separately, but not simultaneously.

From the standpoint of simulations, (52) and (53) are tightly coupled and solved for both of the macroscopic electrochemical potentials simultaneously.

On the other hand, the macroscopic governing equations are given as follows:

$$\nabla\cdot\tilde{\boldsymbol{\sigma}} + \tilde{\rho}\tilde{\boldsymbol{b}} = \boldsymbol{0} \tag{54}$$

$$\tilde{\boldsymbol{\varepsilon}} = \tilde{\boldsymbol{\varepsilon}}^{\mathrm{e}} + \tilde{\boldsymbol{\varepsilon}}^{\mathrm{c}} + \tilde{\boldsymbol{\varepsilon}}^{\theta} + \tilde{\boldsymbol{\varepsilon}}^{\mathrm{r}} \tag{55}$$

$$\tilde{\boldsymbol{\sigma}} = \tilde{\mathbb{C}}\colon\tilde{\boldsymbol{\varepsilon}}^{\mathrm{e}} = \tilde{\kappa}\left(\mathrm{tr}\tilde{\boldsymbol{\varepsilon}}^{\mathrm{e}}\right)\boldsymbol{1} + 2\tilde{\mu}\tilde{\boldsymbol{e}}^{\mathrm{e}} \tag{56}$$

$$\dot{\boldsymbol{\varepsilon}}^{\mathrm{c}} = \dot{\tilde{\gamma}}\frac{\tilde{\boldsymbol{s}}}{||\tilde{\boldsymbol{s}}||} \tag{57}$$

$$\dot{\tilde{\gamma}} = C_1|\bar{\sigma}|^{C_2}\exp\left(-\frac{C_3}{\tilde{\theta}}\right) \tag{58}$$

$$\boldsymbol{\varepsilon}^{\theta} = \Delta\tilde{\theta}\tilde{\boldsymbol{\alpha}} \tag{59}$$

$$\boldsymbol{\varepsilon}^{\mathrm{r}} = \Delta\tilde{\delta}\tilde{\boldsymbol{\beta}} \tag{60}$$

along with the Dirichlet and Neumann conditions on the boundaries Γ_u and Γ_t, respectively, as

$$\tilde{\boldsymbol{u}} = \bar{\boldsymbol{u}} \quad \text{on } \Gamma_u \tag{61}$$

$$\tilde{\boldsymbol{t}} = \tilde{\boldsymbol{\sigma}}\tilde{\boldsymbol{n}} = \bar{\boldsymbol{t}} \quad \text{on } \Gamma_t \tag{62}$$

Here, the indication of symbol $\tilde{\bullet}$ is the same as before.

4 Microstructures of anode and cathode electrodes

We employ $La_{0.6}Sr_{0.4}Co_{0.2}Fe_{0.8}O_{3-\delta}$ (LSCF) for the cathode, 8 mol% yttria-stabilized zirconia (8YSZ) for the electrolyte, Ni–YSZ cermet for the anode, and $La(Ca)CrO_3$ (LCCr) for the interconnect in this study. It is noted that the formulation presented below does not limit target cells, meaning that the component materials can be changed depending on arbitrary target cells.

4.1 Time-variation of Ni–YSZ cermet microstructure

In this study, we assume that the main factor that deteriorates the anode made by Ni–YSZ is the sintering of Ni particles, which aggregate during the steady operation at 973–173 K. In particles touching with each other at lower temperature than the melting point, material transfer occurs so as to reduce the surface energy of the system. With the driving force of the surface energy, the shapes of particles change with time.

To simulate such a time-variation, a phase-field model for sintering [25,27,28,36,37] is employed in this study.

4.1.1 Phase field method

Denoting the order parameters ϕ_1, ϕ_2 and ϕ_3 by the phases of Ni, YSZ and voids, respectively, we employ the following free energy of the Gizburg–Landau-type [42]:

$$F = \int_V \left[\sum_{\mathrm{i}} \frac{1}{2}\alpha_{\mathrm{i}} \|\nabla\phi_{\mathrm{i}}\|^2 + \sum_{\mathrm{i}} A_{\mathrm{i}}\phi_{\mathrm{i}}^2 (1-\phi_{\mathrm{i}})^2 + \sum_{\mathrm{i}} B_{\mathrm{i}}\phi_{\mathrm{i}}^2 + \sum_{\mathrm{i}} \left(\sum_{\mathrm{i}\neq\mathrm{j}} \frac{\beta_{\mathrm{ij}}}{4}\phi_{\mathrm{i}}^2\phi_{\mathrm{j}}^2 \right) + \frac{\gamma}{2}\phi_{\mathrm{i}}^2\phi_{\mathrm{j}}^2\phi_{\mathrm{k}}^2 \right] \mathrm{d}V \tag{63}$$

where index i takes 1, 2 or 3, which indicates the phase of Ni, YSZ or voids. Here, the first and second terms are the surface energies, the third term is the chemical free energy, the fourth term is the interface energy between phases i and j and fifth term is the energy of the TPB. Also, coefficients $\alpha_{\mathrm{i}}, A_{\mathrm{i}}, B_{\mathrm{i}}, \beta_{\mathrm{ij}} = \beta_{\mathrm{ji}}$ and γ are sorts of material constants associated with the corresponding energies or potentials. Since ϕ_{i} are conservative quantities, we adopt the following Cahn–Hilliard equation for their evolutions [43,44]:

$$\frac{\partial\phi_{\mathrm{i}}}{\partial t} = \nabla\cdot\left\{ M_{\mathrm{i}}(\phi_{\mathrm{i}},\theta)\left(\nabla\frac{\delta F}{\delta\phi_{\mathrm{i}}}\right)\right\} \tag{64}$$

where $M_{\mathrm{i}}(\phi_{\mathrm{i}},\theta)$ is the mobility defined as

$$M_{\mathrm{i}}(\phi_{\mathrm{i}},\theta) = D(\phi_{\mathrm{i}})m_{\mathrm{i}}(\theta) \tag{65}$$

Here, $D(\phi_{\mathrm{i}})$ and $m_{\mathrm{i}}(\theta)$ are the diffusivity function and the mobility function that depends on temperature, respectively, and are defined as [37,42]:

$$D(\phi_{\mathrm{i}}) = D_{\mathrm{vol}} f(\phi_{\mathrm{i}}) + D_{\mathrm{vap}}(1-f(\phi_{\mathrm{i}})) + D_{\mathrm{surf}}\phi_{\mathrm{i}}(1-\phi_{\mathrm{i}}) \tag{66}$$

$$m_{\mathrm{i}}(\theta) = \frac{10^8}{2}\left(1+\tanh\frac{\theta-a_{\mathrm{i}}}{b_{\mathrm{i}}}\right) \tag{67}$$

where D_{vol}, D_{vap} and D_{surf} are the diffusivities for the volumetric diffusion, the gas diffusion and the surface diffusion, respectively, and a_{i} and b_{i} are the mobility parameters. Also, we assume $f(\phi_{\mathrm{i}})$ takes the following form:

$$f(\phi_{\mathrm{i}}) = \phi_{\mathrm{i}}^3\left(10-15\phi_{\mathrm{i}}+6\phi_{\mathrm{i}}^2\right) \tag{68}$$

Substituting (65) into (64) yields the following evolution equation:

$$\frac{\partial\phi_{\mathrm{i}}}{\partial t} = m_{\mathrm{i}}(\phi_{\mathrm{i}})\left[\left(\nabla D(\phi_{\mathrm{i}})\right)\cdot\left(\nabla\frac{\delta F}{\delta\phi_{\mathrm{i}}}\right) + D(\phi_{\mathrm{i}})\left(\nabla^2\frac{\delta F}{\delta\phi_{\mathrm{i}}}\right)\right] \tag{69}$$

in which the functional derivative $\delta F/\delta\phi_{\mathrm{i}}$ can be calculated as (See Appendix 1)

$$\frac{\delta F}{\delta\phi_{\mathrm{i}}} = A_{\mathrm{i}}\left(2\phi_{\mathrm{i}} - 6\phi_{\mathrm{i}}^2 + 4\phi_{\mathrm{i}}^3\right) + 2B_{\mathrm{i}}\phi_{\mathrm{i}} + \beta_{\mathrm{ij}}\phi_{\mathrm{j}}^2\phi_{\mathrm{i}} + \gamma\phi_{\mathrm{j}}^2\phi_{\mathrm{k}}^2\phi_{\mathrm{i}} - \alpha_{\mathrm{i}}\nabla^2\phi_{\mathrm{i}} \tag{70}$$

Discretizing (69) with the finite difference method, we can easily simulate the temporal developments of the order parameters (See Appendix 2).

4.1.2 Simulation of Ni-sintering

Figure 4 shows the microscopic analysis models of anode (Ni–YSZ) and cathode (LSCF) microstructures, which are generated by the 3-dimensional porous material simulator POCO [45], though other methods such as [46] are available. A phase-field simulation with the above-described evolution

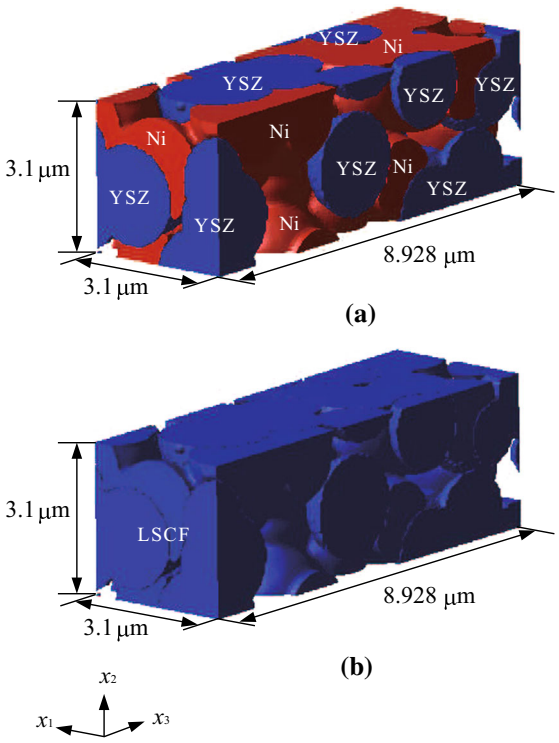

Fig. 4 Microscopic analysis model of porous electrodes. **a** Microscopic model of anode. **b** Microscopic model of cathode

equations is carried out only for the Ni particles in Fig. 4a that are assumed to be exclusively sintered.

The finite difference model is generated with $50\times50\times146$ grids ($\Delta x\times\Delta y\times\Delta z = 0.062\,\mu\text{m}\times0.062\,\mu\text{m}\times0.062\,\mu\text{m}$). The material constants are chosen as $\alpha_1 = \alpha_2 = 14.0\times10^{-2}\,\text{J/cm}^3$, $A_1 = A_2 = 22.0\times10^{-3}\,\text{J/cm}^3$, $B_1 = B_2 = 1.0\,\text{J/cm}^3$, $\beta_{12} = 5.0\times10^{-3}\,\text{J/cm}^3$, $\beta_{13} = \beta_{23} = 0.0\times$ J/cm^3, $\gamma = 100.0\times10^{-3}\,\text{J/cm}^3$, $D_{\text{vol}} = 5.0\times10^{-13}\,\text{cm}^2/\text{s}$, $D_{\text{vap}} = 5.0\times10^{-15}\,\text{cm}^2/\text{s}$ and $D_{\text{surf}} = 2.0\times10^{-10}\,\text{cm}^2/\text{s}$. It is noted here that the diffusivity of the interface is set at a value larger than the ones for the solid and gas phases to promote the sintering near the interfaces [37]. Figure 5 is the schematic of the condition of temperature control in a virtual SOFC operation. After the temperature increases to 1073 K, this constant value of temperature is kept for 11 h, and then decreases to the room temperature by natural cooling. Under this temperature control, the sintering simulation is assumed to start when the temperature reaches at 1073 K, since Ni particles are sintered mainly in steady operations [1]. Here, the simulation time is 11h with $\Delta t = 1$ s.

Microstructures of anode and cathode electrodes should be different in reality. Grain sizes may differ for the same anode material. It can be said for cathode material. However, it is known that the geometrical configurations of anode and cathode microstructures must be similar and that the grain sizes, which are about 0.1–10.0 μm in the realistic materials (For example [47,48]), are most likely comparable. In this sense, it is reasonable to assume for the sake of simplicity that the same microstructure can be used for anode and cathode electrodes in the present numerical simulations, even though the constituent materials are different. Therefore, it is expected that this assumption does not make the simulated results unrealistic.

The results of the sintering simulation of Ni particles are provided in Fig. 6 that shows the time-variation of the anode microstructure with the TPBs, which are generation sites of reaction currents. The corresponding time-variation of the amount of the TPBs is shown in Fig. 7, revealing that the frequency of TPBs is reduced with time during the sintering of Ni particles.

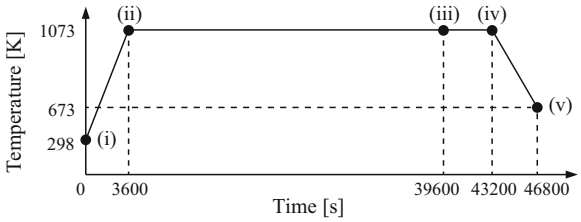

Fig. 5 Condition of temperature control

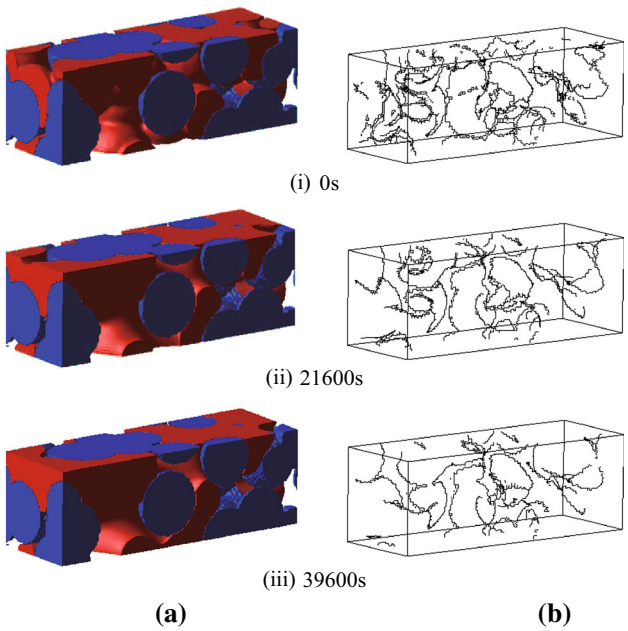

Fig. 6 Time-variation of microstructures **a** Time-varying geometry of Ni. **b** Distribution of TPBs

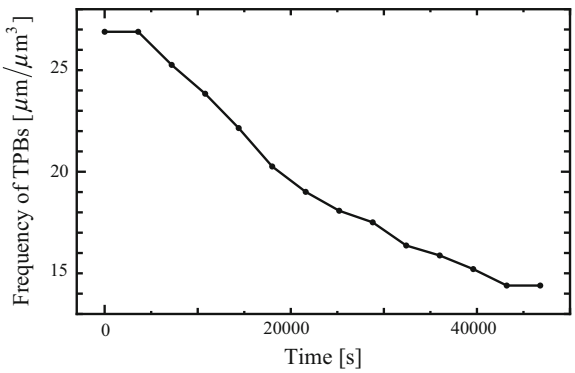

Fig. 7 Temporal change of frequency of TPBs

4.2 Material properties

To evaluate the macroscopic material properties of the anode and cathode electrodes by performing the homogenization analyses, the material properties of the constituents of the anode and cathode microstructures have to be acquired in advance. For that purpose, we have conducted necessary experiments and literature searching to obtain the data presented in Table 1 [38–41] for electric conductivities, Table 2 [38,39] for the relationship between the oxygen vacancy and oxygen potential, Table 3 for the molal volume, Table 4 for the elastic properties, and Table 5 [6,39,49–52] for the CTE and CRE.

Here, the values of electric conductivities $\sigma_{O^{2-}}$ and σ_{e^-} provided in Table 1 are used in (52) and (53). Also, the values of capacitances $c_{O^{2-}}$ and c_{e^-} for LSCF and LCCr are determined with (14) and the relationships provided in Table 2, while those of 8YSZ and Ni–YSZ are set at $1.0\times10^3\,\text{F/cm}^3$.

Table 1 Electronic and oxygen ionic conductivities [38–41]

	σ_{e^-}	$\sigma_{O^{2-}}$
LSCF (Cathode)	$354.45 - 2379.7\delta$	$\frac{4F^2}{V_m}\frac{D_v\delta}{R\theta}$ $D_v = 3.0\times10^{-1}\exp\left(-\frac{99280}{R\theta}\right)$
8YSZ (Electrolyte)	$1.31\times10^7\exp\left(-3.88\frac{F}{R\theta}\right)p_{O^2}^{-1/4}$	$1.63\times10^2\exp\left(-0.79\frac{F}{R\theta}\right)$
Ni–YSZ (Anode)	$\sigma_{e^-}^{YSZ} = 6.6\times10^2\exp\left(-1.9\frac{e}{k\theta}\right)p_{O^2}^{-1/4}$ $+3.7\times10^6\exp\left(-3.7\frac{e}{k\theta}\right)p_{O^2}^{-1/4}$ $\sigma_{e^-}^{Ni} = 1.45\times10^4$	$\frac{9.7\times10^5}{\theta}\exp\left(-\frac{e}{k\theta}\right)$
LCCr (Interconnect)	$p_{O_2} = \frac{\{(6+x)\mu F-\sigma_{e^-}V_m\}^2(\sigma_{e^-}V_m)^4}{K_{0x}^2(x\mu F-\sigma_{e^-}V_m)^2(\mu F-\sigma_{e^-}V_m)^4}$ $\mu = \frac{267.28086}{\theta}\exp\left(-\frac{11584.73}{R\theta}\right)$ $K_{0x} = \frac{0.000155}{\theta}\exp\left(-\frac{261026.3}{R\theta}\right)$	$\frac{4F^2}{V_m}\frac{D_v\delta}{R\theta}$ $D_v = 0.028883\exp\left(-\frac{76571.94}{R\theta}\right)$

Table 2 Relationship between oxygen potential and vacancy [38,39]

LSCF (Cathode)	$\log\ p_{O_2}\log\left(\frac{(3-\delta)^2([Sr]-2\delta)^4}{\delta^2\exp\left(\frac{-2(h_0-\theta s_0)}{R\theta}\right)}\exp\left(\frac{2(a_0k+\theta)}{R\theta}\right)\right)$ $h_0 = -79553\,\mathrm{J/mol}$, $s_0 = -48.54\,\mathrm{J/(mol\cdot K)}$, $a_0 = -610990\,\mathrm{J/mol}$, $k = 512.06\,\mathrm{J/(mol\cdot K)}$, $[Sr] = 0.4$
8YSZ (Electrolyte)	Almost no oxygen vacancy
Ni–YSZ (Anode)	Almost no oxygen vacancy
LCCr (Interconnect)	$p_{O_2} = \left[\frac{1}{K}\left(\frac{3-\delta}{\delta}\right)\left(\frac{x-2\delta}{1-x+2\delta}\right)^2\exp\left(\frac{a\delta}{R\theta}\right)\right]^2$ $K = 4.227\times10^{-3}\exp\left(\frac{218410}{R\theta}\right)$, $a = 407.22\theta - 430048$, $x = [Ca] = 0.3$

Table 3 Molal volume

	Molar mass (g/mol)	Mass density (g/cm^3)	Molal volume (g/cm^3)
LSCF	222.85	6.36	35.04
8YSZ	121.67	5.94	20.48
LCCr	209.26	6.10	34.30

Table 4 Elastic properties

	Young's modulus (GPa)	Poisson's ratio
Ni	200	0.31
YSZ	210	0.30
LCCr	46.5–62.8	0.30

Table 5 Coefficients of thermal and reduction-induced expansions [6,39,49,51,52]

	CTE	CRE
LSCF	1.20×10^{-5}	6.66×10^{-2}
8YSZ	1.07×10^{-5}	—
Ni	1.34×10^{-5}	—
YSZ	1.05×10^{-5}	—
LCCr	1.00×10^{-5}	2.60×10^{-2}

The values of $\Delta\tilde{\delta}$, which is used in (60) to evaluate the reduction-induced strain, can also be determined with these relationships in Table 2. Moreover, the Young's moduli and Poisson's ratios of LSCF and 8YSZ are known to reveal the dependency on the temperature as shown in Fig. 8a, b, whereas those of Ni, YSZ and LCCr are assumed to be constant as provided in Table 4.

5 Homogenization: numerical material testing

With the geometrical and material information about the anode and cathode microstructures at hand, NMTs [34] are conducted to evaluate the macroscopic or homogenized material properties. The homogenized properties to be calculated here are the macroscopic electronic and oxygen-ionic conductivities, the macroscopic elastic constants, creep parameters and CTE. In particular, we have to carry out the homogenization analyses for the anode microstructure made of Ni–YSZ cermet by taking into account the time-variation of its micro-scale geometry due to the Ni-sintering that has been studied in the previous section. It is to be noted that the periodic BCs are not assumed for the homogenization analy-

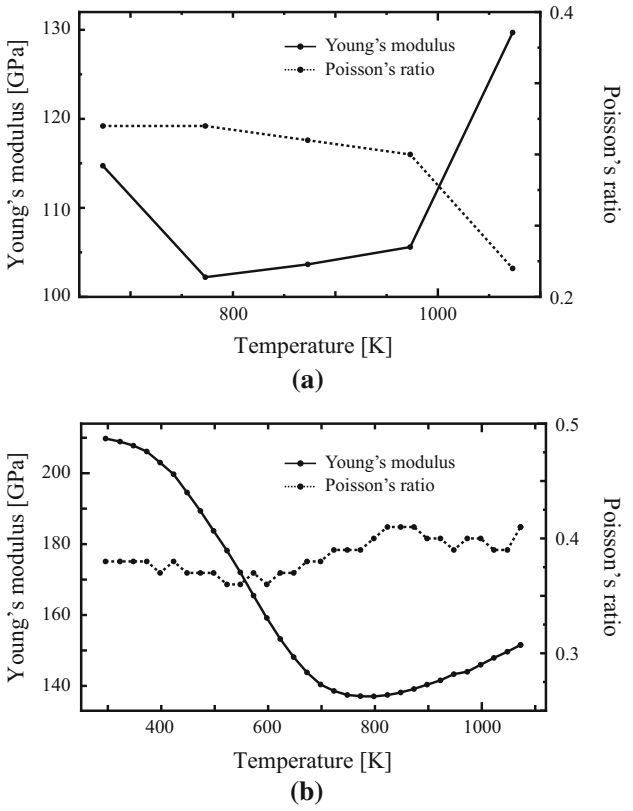

Fig. 8 Temperature-dependent Young's moduli and Poisson's ratios. **a** LSCF. **b** 8YSZ

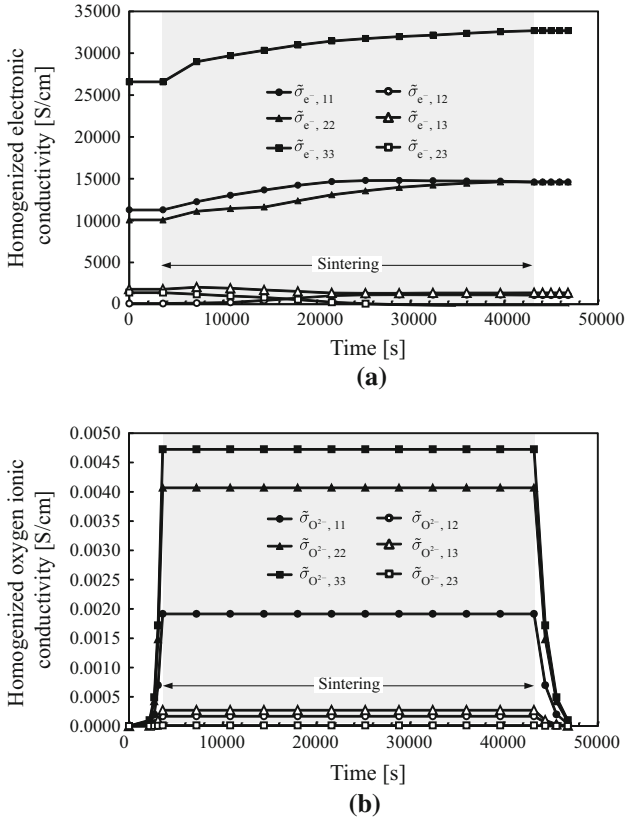

Fig. 9 Temporal change in homogenized conductivities of Ni–YSZ. **a** Temporal change in homogenized electronic conductivity. **b** Temporal change in homogenized oxygen ionic conductivity

ses conducted in this section, since the microstructures under consideration do not have geometrical periodicity. Instead, we take the Dirichlet BCs to evaluate both the macroscopic electronic and elastic properties.

5.1 Linear homogenization for Ni–YSZ cermet

On the basis of (33)–(43), NMTs are conducted for the analysis model of the anode microstructure, whose initial configuration is provided in Fig. 4. Since the time-variation of its geometry due to the Ni-sintering has been obtained in the previous section and is provided in Fig. 6, some configurations at selected time steps are used for computational models in the homogenization analyses under the same condition of temperature control as that of the sintering process (see Fig. 5).

The calculated conductivities of electron and oxygen ion are provided in Fig. 9a, b, respectively. As can be seen from Fig. 9a, the components of the homogenized electronic conductivity increase from 3600s to 43200s due to the aggregation of Ni particles, which are the main media for electronic conduction. On the other hand, the components of the homogenized oxygen-ionic conductivity reveal almost constant values during the sintering process of Ni

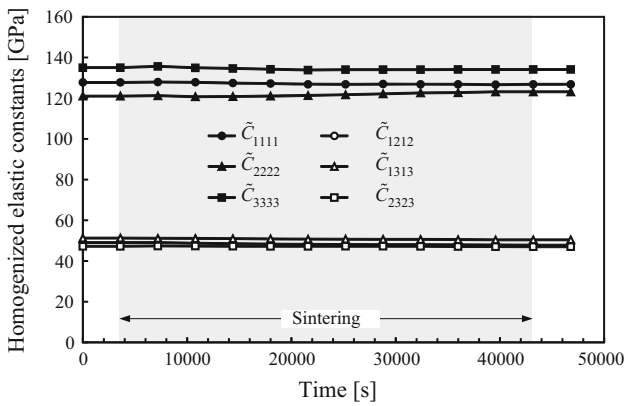

Fig. 10 Temporal change in homogenized elastic constants of Ni–YSZ

particles, reflecting the fact that the oxygen ions conduct in the YSZ phase whose geometry has not been changed with time (Fig. 9b). Also, the homogenized electronic conductivity is not sensitive to the temperature change, while the oxygen-ionic conductivity exhibits strong dependency on the temperature change, which can be observed from 0s to 3600s and from 43200s to 46800s.

The calculated homogenized elastic coefficients of the anode electrode are provided in Fig. 10. In this figure, mod-

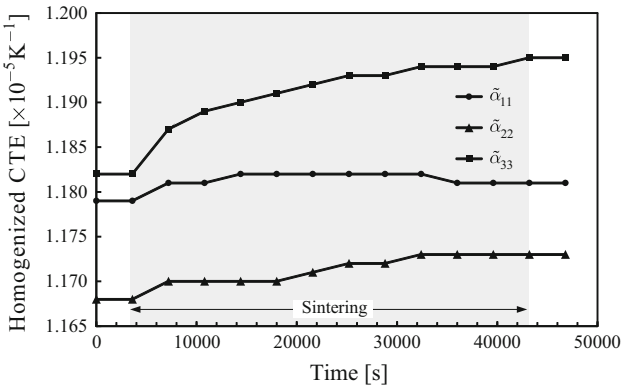

Fig. 11 Temporal change in homogenized CTE of Ni–YSZ

erate reductions during the Ni-sintering are observed in these values.

Figure 10 shows the time-variation of macroscopic elastic constants due to the time variation of the micro-scale geometries caused by sintering, which does not reflect the creep behavior. It is noted that the creep deformation is also assumed during the sintering process, but at the same time its characteristic is affected by the sintering, which is illustrated in Fig. 15.

Figure 11 shows the time-variation of the homogenized CTE of the anode electrode, which reveals an increasing trend during the Ni-sintering process. This is probably due to the fact that the CTE of Ni is larger than that of YSZ as shown in Table 5.

5.2 Linear homogenization for cathode made of LSCF

The computational model for the cathode made of LSCF is shown in Fig. 4b whose geometry is assumed not to change with time. The condition of temperature control is the same as before. The homogenized conductivities of electron and oxygen ion in the cathode are calculated by means of the linear homogenization formulae and provided in Fig. 12a, b, respectively. As can be seen from these figures, they depend on the temperature and the oxygen vacancy, reflecting the material behavior assumed for the constituents in the cathode microstructure.

On the other hand, the homogenized elastic properties evaluated in the NMTs depends on the temperature change as can be seen in Fig. 13. This trend is similar to that of the anode made of Ni–YSZ cement, which is shown in Fig. 8a.

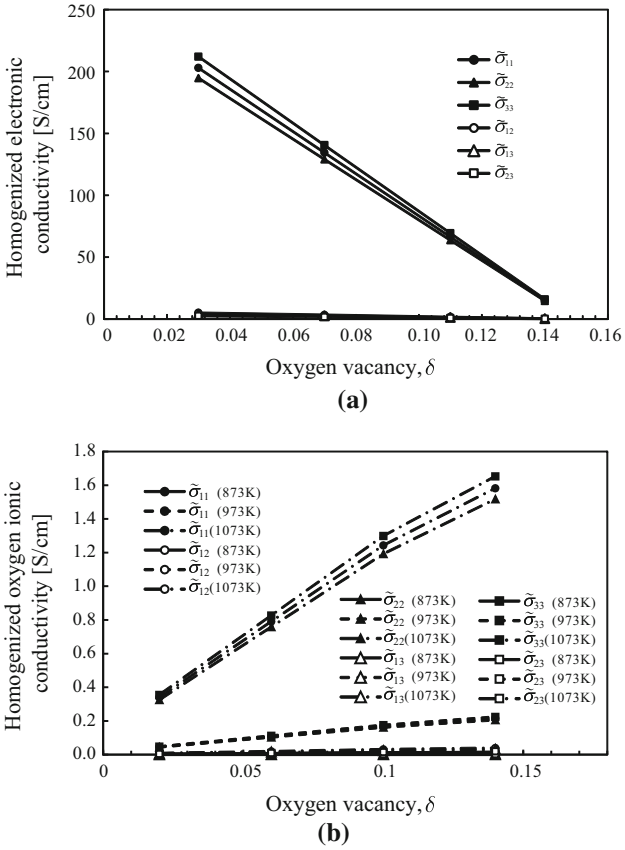

Fig. 12 Dependency of homogenized conductivities of LSCF on oxygen vacancy. **a** Homogenized electronic conductivity. **b** Homogenized oxygen ionic conductivity

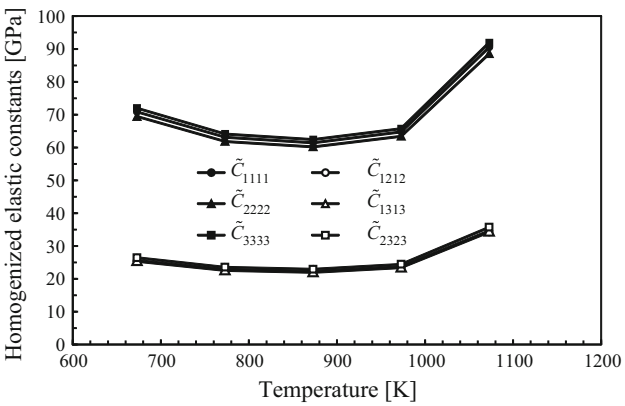

Fig. 13 Dependency of homogenized elastic constants of LSCF on temperature

5.3 Nonlinear homogenization for creep properties

Since the formulation for linear homogenization cannot be applied to the creep material behavior of the anode and cathode electrodes, the parameter identification has to be conducted after the NMTs. More specifically, we have to perform an optimization process based on (28) to identify the homogenized creep parameters by using appropriate sets of macroscopic stress–strain curves that can be obtained by a series of NMTs . In this study, we employ the method of particle swarm optimization (PSO) that has been used successfully in [34].

First, we are concerned with the creep properties of the anode electrode made of Ni–YSZ cermets. The experiments have been conducted for YSZ and Ni to obtain the stress relaxation curves provided in Fig. 14a, b. Then, their creep parameters are respectively identified as follows:

YSZ: $C_1 = 1.0 \times 10^{-15}$, $C_2 = 5.8$ and $C_3 = 4.0 \times 10^3$
Ni: $C_1 = 1.0 \times 10^{-8}$, $C_2 = 2.7$ and $C_3 = 4.5 \times 10^3$

It can be found that the stress relaxation or creep characteristic of Ni becomes more significant than that of YSZ with an increase of temperature. In particular, the stress is rapidly relaxed within a few tens of minutes at 1073 K. Using these data along with the elastic properties provided in Table 4, we conduct NMTs on the same computational models used in Sect. 5.1, some of which reflects the effect of Ni-sintering during t = 3600–43200s. The obtained macroscopic stress–strain curves are depicted by solid lines in Fig. 15, and used as the data for the PSO to identify the homogenized creep parameters that are given in Table 6. The dotted lines in Fig. 15 are the macroscopic stress–strain responses calculated with the identified parameters.

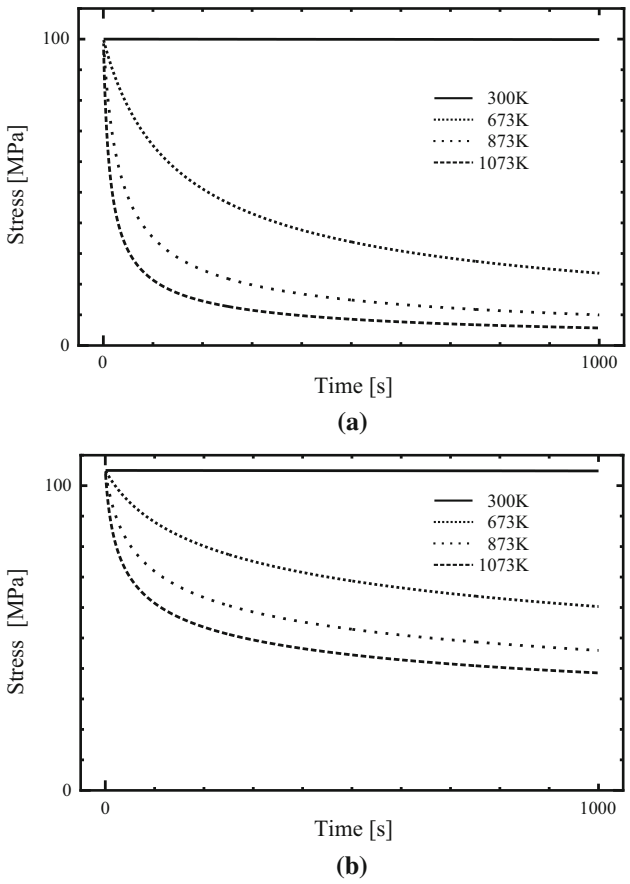

Fig. 14 Creep property of Ni and YSZ: stress relaxation curves. **a** Ni. **b** YSZ

The macroscopic stress–strain curves in Fig. 15, which exhibit typical strain-rate dependency, are obtained for identifying the creep parameters in the numerical material tests and do not show the actual behavior during the SOFC operation. Each curve reflects the creep characteristics for the corresponding micro-scale geometry subjected to the sintering of Ni and the ambient temperature.

Next, we consider the cathode electrode made of LSCF whose creep parameters are set at $C_1 = 1.0 \times 10^{-15}$, $C_2 = 5.8$ and $C_3 = 4.0 \times 10^3$ and temperature-dependent elastic properties are given in Fig. 8a. Using these values in the computational model in Fig. 4b, we conduct the NMTs to obtain the macroscopic stress–strain curves as shown in Fig. 16. The creep parameters identified by the PSO are provided in Table 7 and the identified stress–strain curves are depicted with dotted lines in Fig. 16.

6 Macroscopic analysis

Using the homogenized material properties evaluated in the previous section, we conduct the macroscopic electric conduction and stress analysis sequentially. The purpose of the macroscopic electric conduction analysis is to obtain the spatial distributions of the oxygen potential that determines the amount of reduction-induced strains. It should be noted that the mechanical behavior of the overall cell structure cannot be predicted for the assessment of its mechanical durability without the potential distribution during the SOFC operation.

6.1 Electric conduction analysis

By conducting the FE computations to solve the set of simultaneous equations, (46)–(51), or equivalently (52) and (53), we evaluate the macroscopic oxygen potential $\tilde{\mu}_{\mathrm{O}}$ as well as the electrochemical potentials of electrons and oxygen ions, $\tilde{\eta}_{\mathrm{O}^{2-}}$ and $\tilde{\eta}_{\mathrm{e}^-}$.

6.1.1 Analysis conditions

The target cell structure is of a cylinder-plate type as shown in Fig. 17. But, assuming that the macroscopic potential distributions are the same along the x_3 axis, we confine ourselves to the cross section on the x_1–x_2 plane, as shown in Fig. 18, in the present numerical analysis. The FE mesh is generated with 500 × 120 voxel-type 3D solid elements, and the height of each voxel in the x_3-direction is set at 50 μm. The macroscopic material properties obtained in the previous section are used for the anode and cathode electrodes. The electrochemical properties in Table 1 are used for the interconnect and electrolyte.

Figure 18 also provides the BCs for the macroscopic electrochemical potentials of electrons and oxygen ions, which

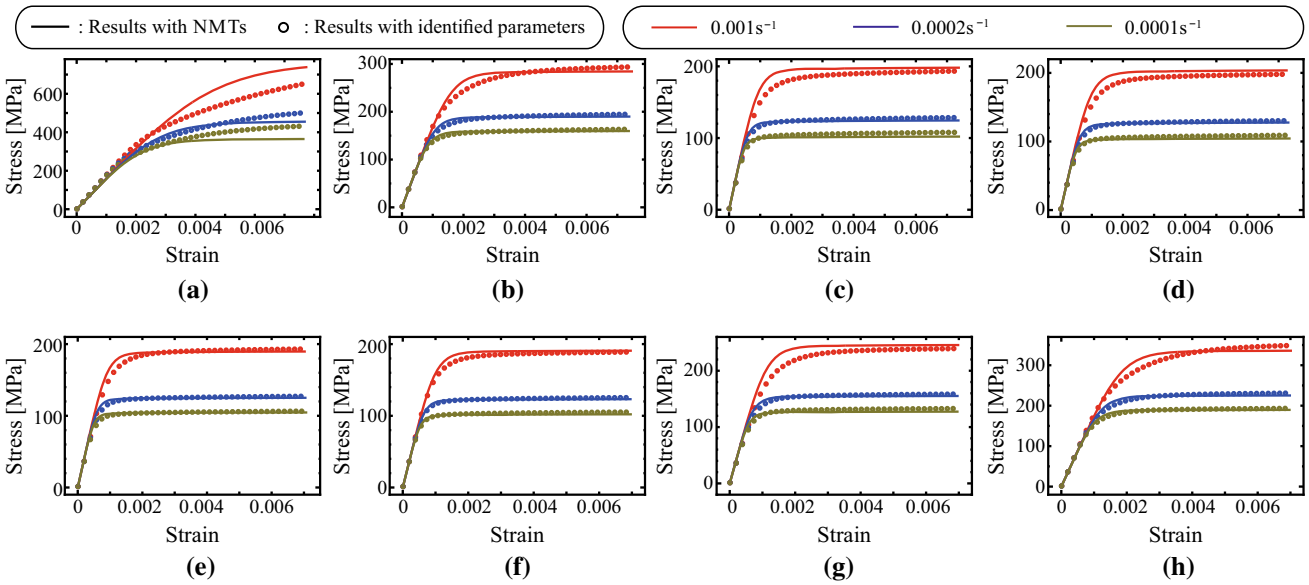

Fig. 15 Stress–strain curves obtained by NMTs and with identified parameters for Ni–YSZ. **a** 0–720 s. **b** 1440–2160 s. **c** 2880–3600 s. **d** 3600–7200 s. **e** 21,600–25,200 s. **f** 39,600–43,200 s. **g** 43,200–45,000 s. **h** 45,000–46,800 s

Table 6 Creep parameters identified for Ni–YSZ

Times (s)	C_1	C_2	C_3
0–720	1.71×10^{-10}	3.50	8305
720–1440	4.22×10^{-10}	3.81	9161
1440–2160	9.79×10^{-10}	4.00	12,170
2160–2880	6.21×10^{-11}	3.76	4534
2880–3600	4.06×10^{-10}	3.46	4127
3600–7200	2.07×10^{-10}	3.61	4351
7200–10,800	3.56×10^{-10}	3.51	4363
10,800–14,400	3.87×10^{-11}	4.05	4838
14,400–18,000	3.37×10^{-10}	3.41	3827
18,000–21,600	2.30×10^{-10}	3.42	3450
21,600–25,200	2.28×10^{-10}	3.75	5254
25,200–28,800	1.37×10^{-10}	3.73	4481
28,800–32,400	1.02×10^{-10}	3.85	4788
32,400–36,000	1.17×10^{-10}	3.68	3834
36,000–36,900	1.83×10^{-10}	3.67	4435
36,900–43,200	3.59×10^{-10}	3.67	5164
43,200–45,000	4.23×10^{-10}	3.51	5344
45,000–46,800	1.33×10^{-8}	4.03	13, 490

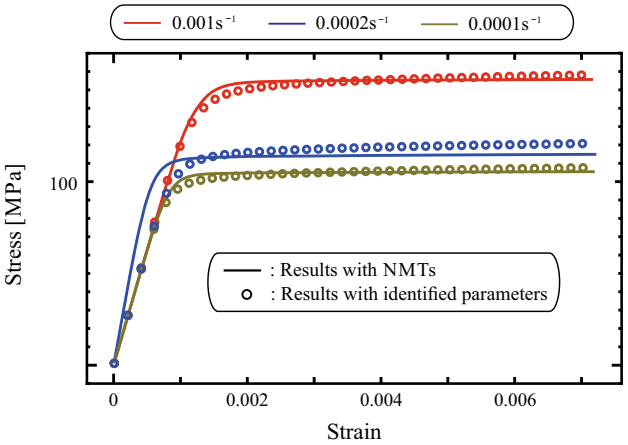

Fig. 16 Stress–strain curves obtained by NMTs and with identified parameters for LSCF

Table 7 Creep parameters of LSCF identified by PSO

Times (s)	C_1	C_2	C_3
0–46,800	3.703×10^{-16}	5.88	1475

assumes the condition of open circuit voltage (OCV). As a condition of earth connection, the electrochemical potentials of electrons is set at zero on the external boundary of the cathode electrode. Therefore, the electric current $\tilde{i}_{e^-}$ on this boundary can be obtained as the solution of the problem, and the corresponding oxygen-ionic current $\tilde{i}_{O^{2-}}$ can be determined with the OCV condition such that $\tilde{i}_{e^-} + \tilde{i}_{O^{2-}} = 0$. On the external boundary of the interconnect, both of the electronic and oxygen-ionic currents are assumed to follow the Neumann type BC, whose functional form is provided in (8) with $\alpha = 0.7$, under the OCV condition. Furthermore, using (3) with $\alpha = 0.3$, we impose almost the same BC as that of the interconnect to the surfaces of fuel channels made in the anode electrode.

Although the fuel, namely hydrogen in this study, is supplied in the fuel channel and diffuses in the porous anode

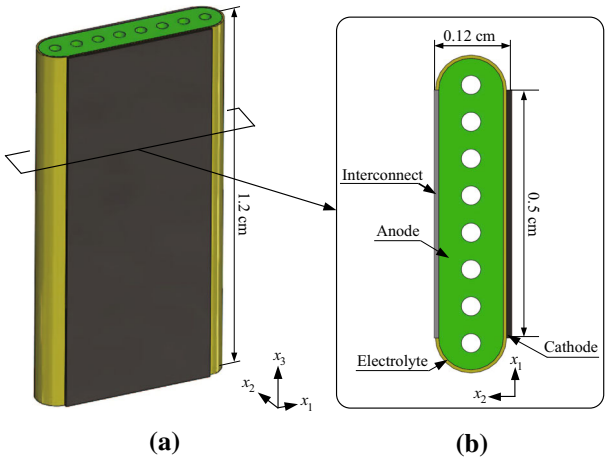

Fig. 17 Macroscopic analysis model for electric conduction problem. **a** Cell structure. **b** In-plane model of cross-section

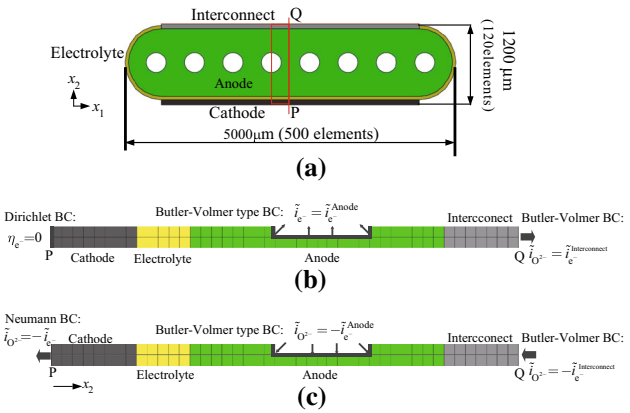

Fig. 18 Boundary conditions of macroscopic electrochemical potential analysis. **a** Cross-section of cylinder-plate type cell. **b** BCs forelectrons. **c** BCs for oxygen ions

electrode in actual situations, it is provided in the anode electrode directly as data of the source term $\tilde{j}_{e^-}$ in (53) in the present computation. Here, the hydrogen's partial pressure is converted to that of the oxygen, and then converted to the oxygen potential using (5) so that the potential difference (4) can be evaluated. This value of the difference is used again in (3) with $\alpha = 0.3$ to determine the reaction current in the anode electrode. This reaction current in the anode, which is assumed to be generated at the TPB, is calculated according to the amount of TPBs and is converted to the source term $\tilde{j}_{e^-}$ with the relationship provided in (45). The time-variation of the amount of TPBs has been evaluated by the phase-field simulation in Sect. 4. On the other hand, the way to calculate the reaction current in the cathode is almost the same as that of the anode under the assumption that the oxygen partial pressure in the cathode is the same as that of the atmosphere and is uniformly distributed in it. The amount of the DPB can be calculated with the geometrical information of the FE model shown in Fig. 4b and is used in (44).

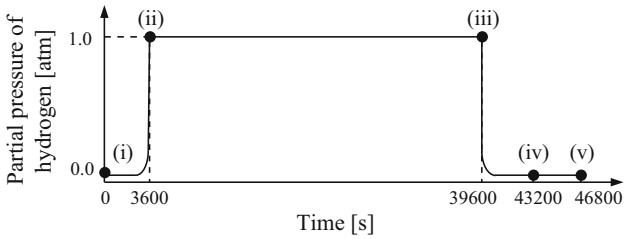

Fig. 19 Supplying condition of hydrogen in anode

The condition of temperature control is the same as that in Fig. 5. Also, the temperature distribution is assumed to be uniform over the analysis domain. The assumed controlling condition of the hydrogen's partial pressure p_{H_2} supplied to the anode is shown in Fig. 19, in which it is increased from 0 to 0.97 atm during the time range between (i) and (ii). After that, the steady state is kept during the time range between (ii) and (iii), and the hydrogen's partial pressure is decreased to 0 atm within 1 h from (iii) to (iv). 1 h after the fuel supply is stopped, the temperature is gradually decreased to 673 K with natural cooling within 1 h. The overall time is 13 h and is descritized with $\Delta t = 1$s in our numerical analysis.

6.1.2 Numerical results

Figures 20 and 21 show the time-variations of the distributions of the electrochemical potentials of electrons and oxygen ions, respectively. The contour plot on the left of each of these figures shows their time-varying distributions in the x_1–x_2 plane, while the graph on the right of each figure shows their time-varying profiles on line P–Q indicated in Fig. 18.

An increase of the uniform distributions of the electrochemical potential of electrons, which can be observed in Fig. 20i, ii, reflects the supplying condition of fuel in the anode in the numerical analysis. After 3600s, the potential is kept constant as can be seen from Fig. 20ii, iii, realizing the steady states. Although the electrochemical potential of electrons in the anode should be decreased after (iv), when the fuel supply is stopped and temperature is decreased, such a phenomenon has not been reproduced in this numerical simulation. This is probably due to the fact that the value of capacitance of Ni–YSZ is assumed to be larger than the actual value for the numerical stability; namely, it has extra four more digits than that of the other materials in the SOFC under consideration. The same phenomenon occurs in the calculation for the oxygen ion. This discrepancy must be overcome in the near future.

On the other hand, it can be seen from Fig. 21 that the electrochemical potential of oxygen ions decreases in the cathode during the fuel supply. After the fuel is fully supplied, which corresponds to Fig. 21ii, the electrochemical potential

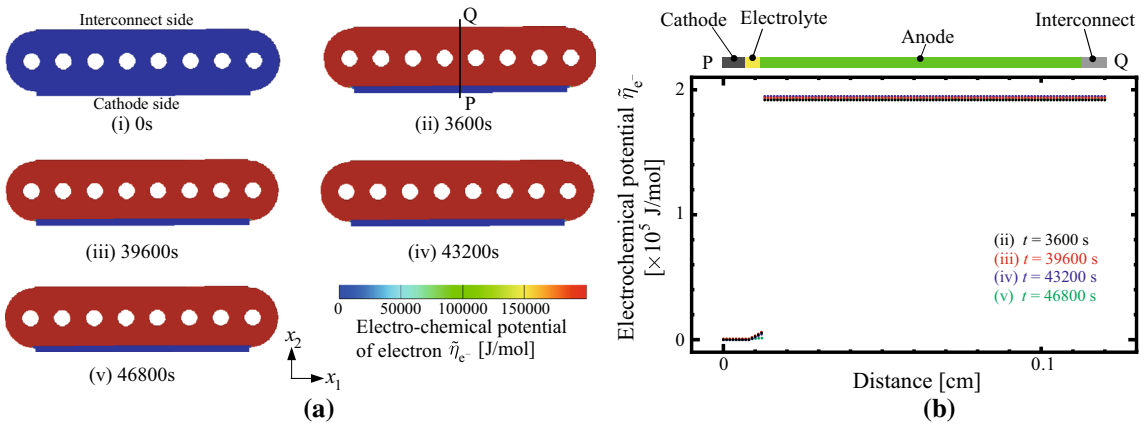

Fig. 20 Temporal changes of electrochemical potential of electron. **a** Distributions of electrochemical potential of electron. **b** Profiles of potential distributions on line P–Q

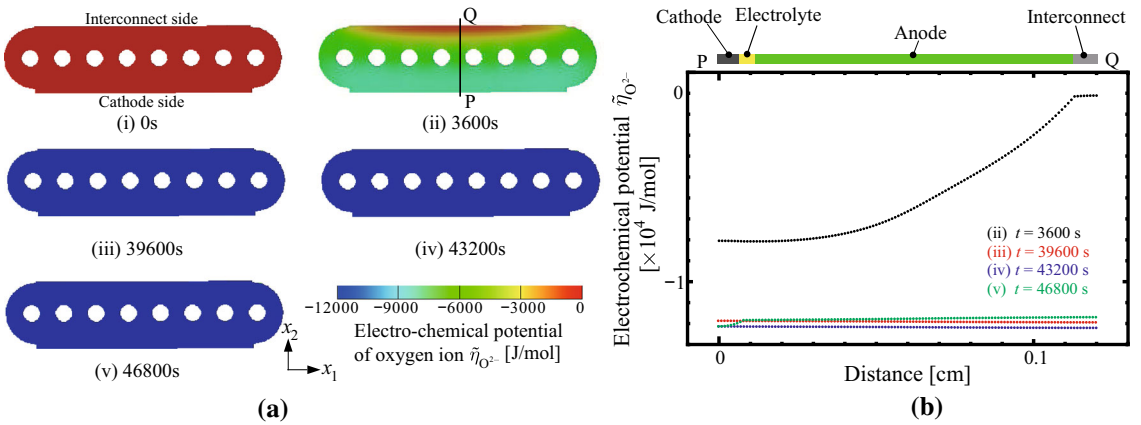

Fig. 21 Temporal changes of electrochemical potential of oxygen ion. **a** Distributions of electrochemical potential of oxygen ion. **b** Profiles of potential distributions on line P–Q

of oxygen ions is more significant at the interconnect side than that at the cathode side. This gradation is attributed to the Butler–Volmer BC at the interconnect side and earth condition at the cathode side. The uniform distribution are found in Fig. 21iii when the cell is filled with the fuel. The changes in the electrochemical potentials in the electrolyte and cathode may contribute to the stress due to reduction-induced expansions.

Figure 22 shows the time-variation of the oxygen potential, which is evaluated with (46) and has an one-to-one relationship with the oxygen vacancy on line P–Q, as shown in Fig. 23. The oxygen vacancy changes during the fuel supply in the cathode and interconnect that have the oxygen non-stoichiometry realized with the relationships in Table 2. In particular, the time-variation of the oxygen vacancy is remarkable in the interconnect, where the time-variation of the oxygen potential is significant. It can be predicted that the stress due to the reduction-induced expansions can be high in cathode and interconnect, since the oxygen vacancies in these components reduce gradually.

Figure 24 shows the distributions of current densities on line P–Q. Here, the blue, red and black lines respectively indicate the electronic, oxygen ionic and total current densities, which satisfy (51). It can be seen from these figures that the electric currents are carried due to the reaction currents in the anode, though the OCV condition are satisfied. For example, the oxygen ionic current is carried from the side with high values of the oxygen ionic potential to the opposite side with low values as seen in Fig. 21b(ii). Relatively high current densities are observed in anode and electrolyte in Fig. 24b, c, which are considered to be the effects of high values of conductivities calculated by the equations in Table 1.

6.2 Stress analysis

Using the homogenized elastic and creep properties, we carry out the stress analysis of the overall cell structure. The quasi-static equilibrium problem was governed by (54)–(60), which are provided in Sect. 3.4. Here, the deformations are caused

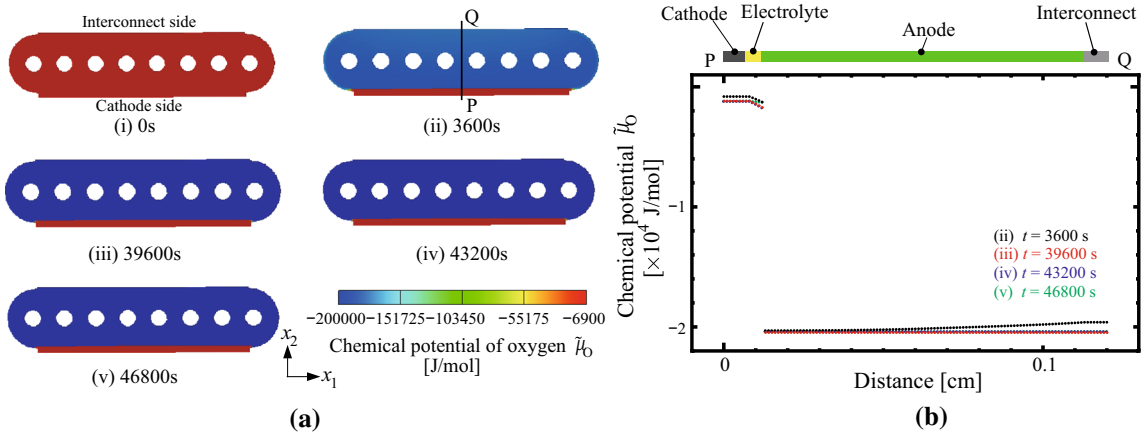

Fig. 22 Temporal changes of chemical potential of oxygen. **a** Distributions of chemical potential of oxygen. **b** Profiles of potential distributions on line P–Q

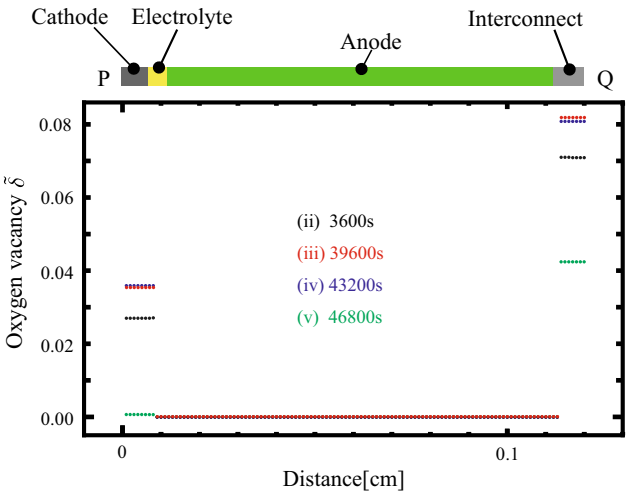

Fig. 23 Temporal change of macroscopic oxygen vacancy profile along line P–Q

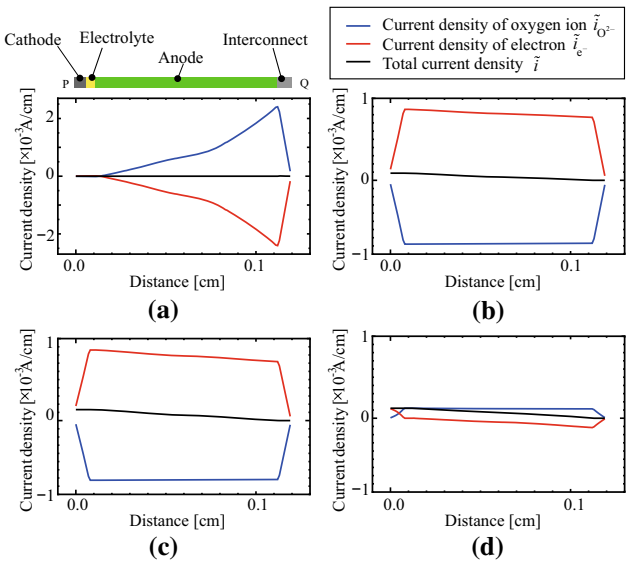

Fig. 24 Temporal change of macroscopic current density profile along line P–Q. **a** 3600 s. **b** 39,600 s. **c** 43,200 s. **d** 46,800 s

mainly by the thermal and reduction-induced strains, $\boldsymbol{\varepsilon}^{\theta}$ and $\boldsymbol{\varepsilon}^{\mathrm{r}}$, the latter of which is determined from the time-variation of oxygen vacancy $\Delta\tilde{\delta}$ obtained in the macroscopic electric conduction analysis conducted in the above.

6.2.1 Analysis conditions

The target of the stress analysis is the overall cell structure and its FE model is provided in Fig. 25 along with the BCs. The FE mesh is composed of $500 \times 120 \times 240$ voxel-type 3D solid elements, each of which is a rectangular parallelepiped of 50μm in height with a 1 μm × 1 μm a square base. The BCs are also provided in Fig. 25, which make this cylinder-plate-type cell be a cantilever beam with the bottom being fixed to the pedestal and without external loading.

The time-variation of the temperature distributions are the same as in the electric conduction analysis in the above (See Fig. 5). Therefore, the thermal strain distributions in the x_1–x_2 cross-section can easily be calculated with temperature change $\Delta\tilde{\theta}$ multiplied by the macroscopic CTEs, which is given in Table 5 and Fig. 11. On the other hand, the time-variation of the reduction-induced strains can be computed from the time-variation of the oxygen vacancy distributions on line P–Q in Fig. 23, which are converted from the oxygen potential distributions with the relationships in Table 2. In the present simulation, $\nabla_y \psi_\delta$ in (36) is neglected so that the macroscopic CRE $\tilde{\beta}$ is the same as β. Thus, the in-plane distributions of the reduction-induced strains in the x_1–x_2 cross-section are calculated with the oxygen vacancy change $\Delta\tilde{\delta}$ multiplied by β. Then, assuming that the same in-plane distributions of the thermal and reduction-induced strains can be set along the x_3 axis, we apply these time-variations to the

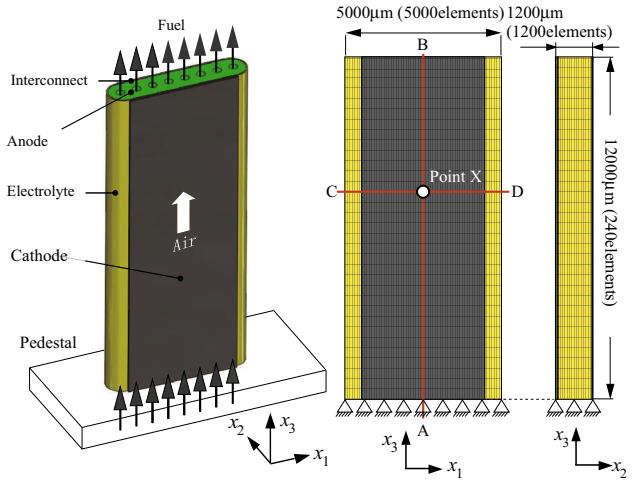

Fig. 25 FE model with boundary conditions for stress analysis

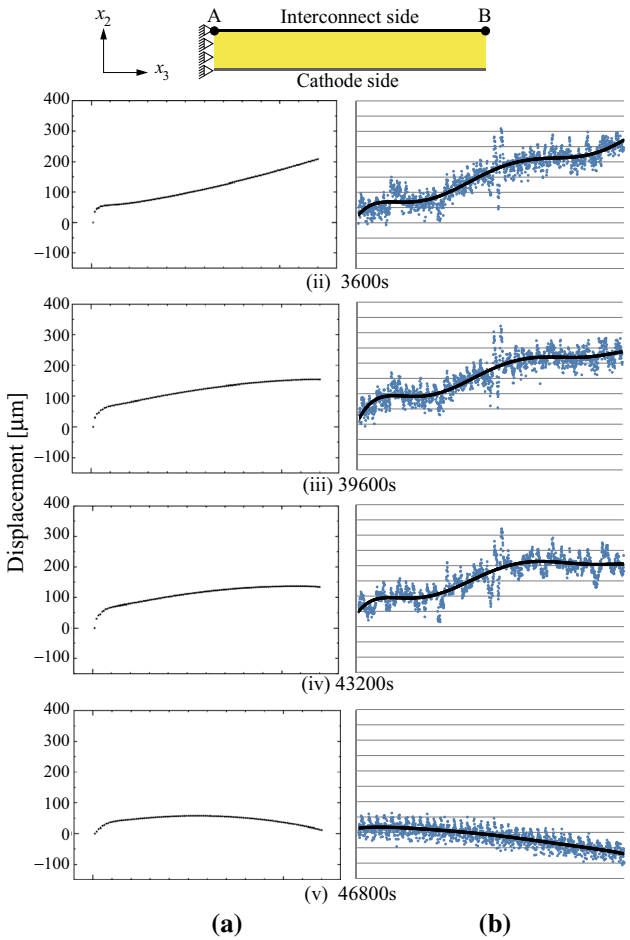

Fig. 26 Temporal change of profiles of x_2-component of displacement along line A–B on interconnect. **a** Analysis results. **b** Experimental results

cell structure as time-varying excitation data. It is noted that the actual size of the cell used in the experiment is much larger than the present numerical model and that the actual operational period is much longer than this analysis. The

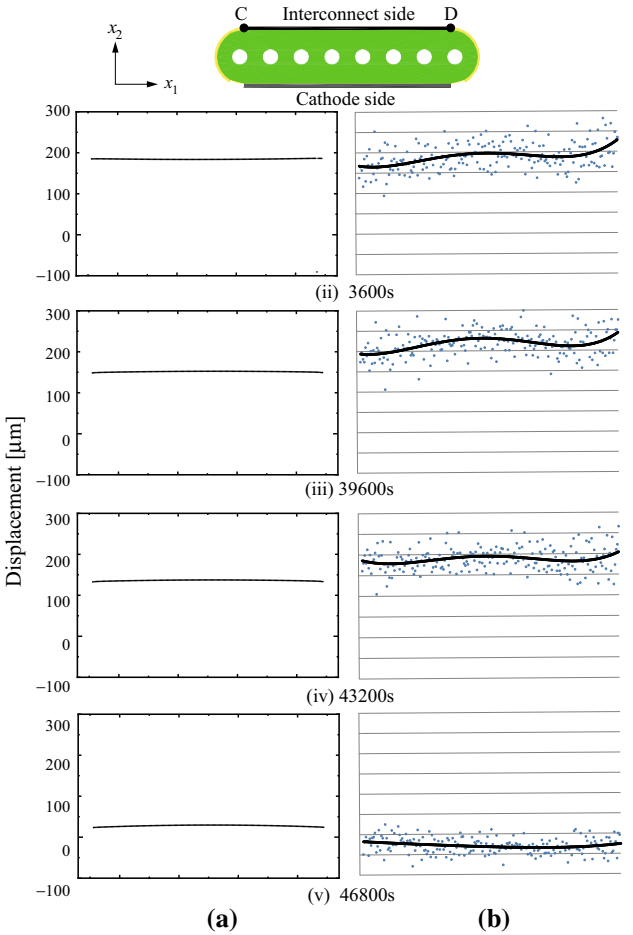

Fig. 27 Temporal change of profiles of x_2-component of displacement along line C–D on interconnect. **a** Analysis results. **b** Experimental results

comparison is made after both the size and the period are converted in view of their homothetic ratios.

6.2.2 Numerical results

Figures 26 and 27 show the comparison of the numerical and experimental results. Figure 26 shows the profiles of the x_2-components of displacement, namely the deflection of the cantilever, along line A–B on the interconnect, while Fig. 27 shows those along line C–D on the interconnect. They are in qualitative agreement. As can be seen from Figs. 26(i) and 27(i), at first, the overall cell structure is bent toward the interconnect side. This initial bending until the temperature reaches at 1073 K has been caused by the significant development of larger thermal expansion strains in the cathode than those in the interconnect. The difference in value of the macroscopic CTEs can be realized shown in Table 5. Subsequently, the deflection is gradually decreased and the head of the cell moves toward the cathode side during 10 h-steady operation and cooling, while the overall shape of the cell

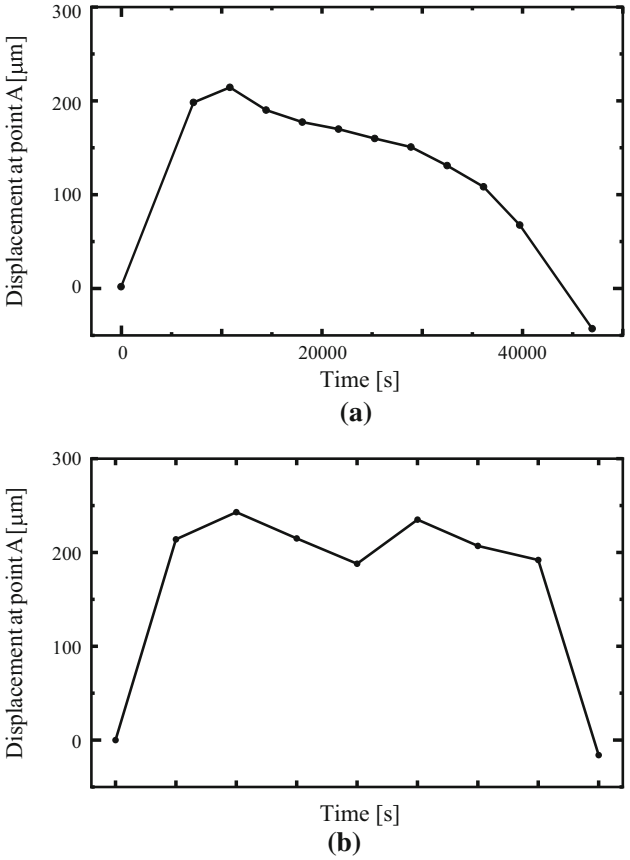

Fig. 28 Temporal change of x_2-component of displacement measured at Point X of intersection of lines A–B and C–D. **a** Simulation result. **b** Experimental result

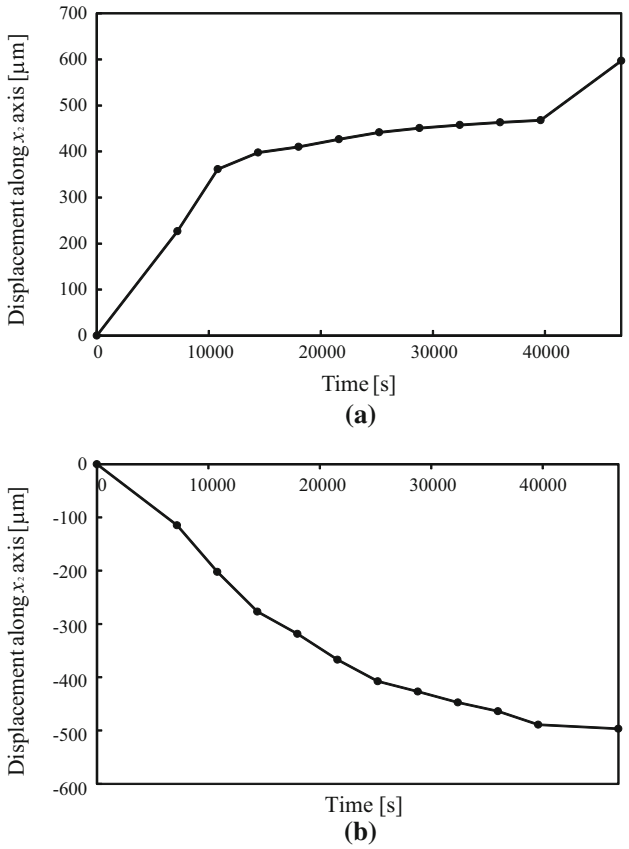

Fig. 29 Temporal change of x_2-component of displacement in cases considering only thermal strain or only reduction strain. **a** Considering only thermal strain. **b** Considering only reduction strain

is warped into the interconnect side [See Figs. 27(ii)–(iv) and 26(ii)–(iv)]. This is probably caused by the reduction-induced expansive strains that are expected to developed in the interconnect side during steady operation and subsequent cooling, as discussed in Sect. 6.1.2.

A similar tendency can be found in the numerical and experimental results shown in Fig. 28a, b, which compare the time-variations of the x_2-components of displacement measured at Point X $(x_1, x_2, x_3) = (0.25, 0.00, 6.40\,\text{cm})$ of intersection of lines A–B and C–D. More specifically, the cell is initially bent towards the interconnect side, and then gradually moves back to the cathode side. Here, the gradual return at a high constant temperature is the effect of creep deformations induced by the internal stress developed by the differences in thermal and reduction-induced strains. Thus, it seems reasonable to conclude that the present procedure for stress analysis enables us to reproduce the mechanical behavior of SOFC under actual start-and-stop operations.

To investigate the effect of reduction-induced deformations, we conducted two additional simulations, in which thermal and reduction-induced strains are separately considered. The results are provided in Fig. 29a, b, respectively. As can be seen from Fig. 29a, the cell is bent toward the interconnect side in the case of no reduction-induced strain, as the thermal strain in the cathode part is more significant than that in the interconnect part. On the other hand, Fig. 29b shows a reverse tendency, in which the cell is bent toward the cathode side, since the reduction-induced deformation of the interconnect is larger than that of the cathode. Clear differences are found between the results of Fig. 29 and that of Fig. 28a. Thus, it can be said that the consideration of reduction-induced deformations is indispensable to conduct the stress analysis for SOFC under operational environment.

Figure 30 shows the deformed configurations of the overall cell structure, which reveals the same trend as discussed above, along with the contours of the x_3-normal stress component. It can be seen from this figure that the stress concentrates at the bottom of the cell and that the stress concentration is gradually relaxed from (ii) to (iii) at a high constant temperature due to creep deformations. However, the compressive stress in the x_3-direction at the bottom changes to the tensile one at the final stage (v), implying the possibility of cracking around the base portion at stopping oprations.

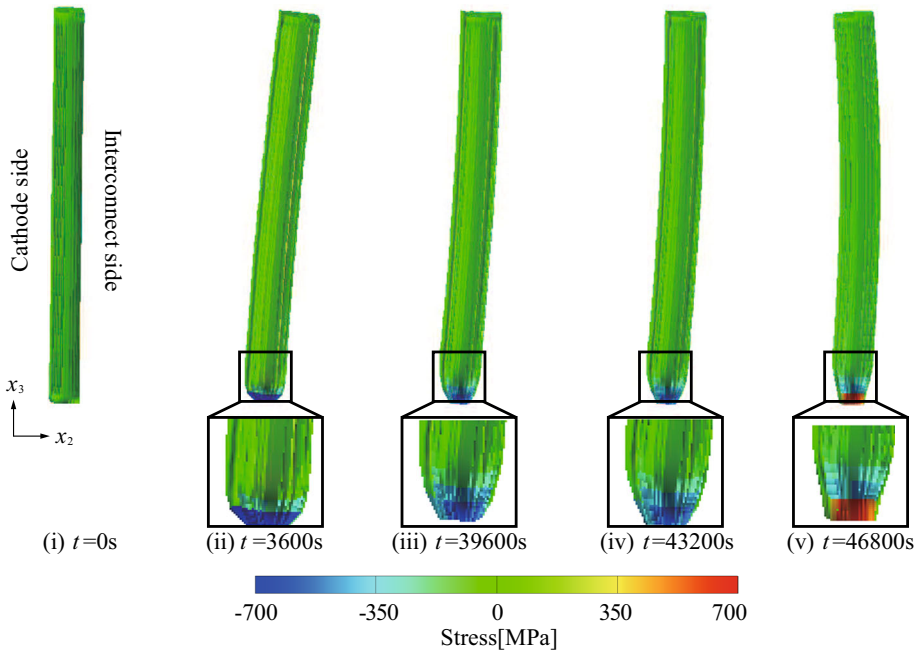

Fig. 30 Temporal change of stress distributions on deformed configurations

Although the effects of Ni sintering have been taken into account in the values of the homogenized mechanical properties, they seem to be little in the present stress analysis for this cell structure. In particular, the displacement in the x_2-direction is hardly affected by the geometrical change of the anode microstructures, since the anode has a symmetrical shape and is located in the axial region of this beam-like cell. However, the effect might be significant depending on the shape design of cells.

7 Conclusions

In this study, to perform stress analyses of SOFCs under operation, we have developed a characterization method of its time-varying macroscopic electro-chemo-mechanical behavior of electrodes by taking into account the time-varying geometries of anode microstructures due to Ni-sintering. The conclusions drawn in this study are summarized as follows:

1. A phase-field method was presented to simulate the micro-scale morphology change with time, from which the time-variation of the amount of TPBs is directly predicted.
2. The numerical material tests based on the homogenization method were conducted for each state of the sintered microstructures, to evaluate the time-variation of the macroscopic oxygen ionic and electronic conductivities and the inelastic properties of the anode electrode.
3. In the homogenization analyses, the dependencies of the properties of constituent materials on temperature and/or the oxygen potential, which is supposed to change within an operation period, were also considered.
4. Under the assumption of an actual start-and-stop operation, the macroscopic electric conduction analysis was conducted to predict the oxygen potential distribution in an overall cell structure under long-period operation with start-and-stop control, which determines reduction-induced expansive/contractive deformation of oxide materials.
5. The macroscopic stress analysis is carried out for the overall SOFC structure with the stress-free strains and the homogenized mechanical properties, both of which depend on the operational environment.
6. The stress analysis results gave good agreement with the experimental data; both of them show similar tendencies of the time-variations of displacement of the overall cell structure.

It should be emphasized that this study presents a new method of two-scale analyses of SOFC under start-and-stop operations that involves multiphysics phenomena. Although the one-way coupling scheme is employed and there are some discrepancies between the assumptions made in the numerical analyses and the actual situations, the method proposed in this study provides at least a new framework of two-scale electro-chemo-mechanical coupling analyses to assess the mechanical durability of SOFC. An emphasis is also placed on the fact that the present method involves general versatility; that is, the formulation of the present

two-scale electro-chemo-mechanical coupling problems in consideration of time-varying microstructures in homogenization analyses can be applied to other types of multi-scale multiphysics problems encountered in practice.

Acknowledgments This work was carried out as a part of the research project "Technology development for SOFC commercialization promotion. Basic study on rapid evaluation method of SOFC durability", which was supported by the New Energy and Industrial Technology Development Organization (NEDO), Japan.

Appendix 1

Usual Ginzburg–Landau type energy can be calculated as follows:

$$F = \int_V \left[g(\rho) + \frac{\alpha}{2} \|\nabla \rho\|^2 \right] \mathrm{d}V \tag{71}$$

The variation of Eq. (71) is calculated as the following [53].

$$\frac{\delta F}{\delta \phi_i} = \frac{\partial g}{\partial \phi_i} - \frac{1}{2}\alpha_i \left\{ \frac{\mathrm{d}}{\mathrm{d}x} \frac{\partial}{\partial (\nabla_x \phi_i)} \|\nabla \phi_i\|^2 + \frac{d}{dy} \frac{\partial}{\partial (\nabla_y \phi_i)} \|\nabla \phi_i\|^2 + \frac{\mathrm{d}}{\mathrm{d}z} \frac{\partial}{\partial (\nabla_z \phi_i)} \|\nabla \phi_i\|^2 \right\} \tag{72}$$

$$\frac{\delta F}{\delta \phi_i} = \frac{\partial g}{\partial \phi_i} - \frac{1}{2}\alpha_i \left[\frac{\mathrm{d}}{\mathrm{d}x} \frac{\partial}{\partial \frac{\partial \phi_i}{\partial x}} \left\{ \left(\frac{\partial \phi_i}{\partial x}\right)^2 + \left(\frac{\partial \phi_i}{\partial y}\right)^2 + \left(\frac{\partial \phi_i}{\partial z}\right)^2 \right\} + \frac{\mathrm{d}}{\mathrm{d}y} \frac{\partial}{\partial \frac{\partial \phi_i}{\partial y}} \left\{ \left(\frac{\partial \phi_i}{\partial x}\right)^2 + \left(\frac{\partial \phi_i}{\partial y}\right)^2 + \left(\frac{\partial \phi_i}{\partial z}\right)^2 \right\} + \frac{\mathrm{d}}{\mathrm{d}z} \frac{\partial}{\partial \frac{\partial \phi_i}{\partial z}} \left\{ \left(\frac{\partial \phi_i}{\partial x}\right)^2 + \left(\frac{\partial \phi_i}{\partial y}\right)^2 + \left(\frac{\partial \phi_i}{\partial z}\right)^2 \right\} \right] \tag{73}$$

$$= \frac{\partial g}{\partial \phi_i} - \alpha_i \left\{ \frac{\mathrm{d}}{\mathrm{d}x}\left(\frac{\partial \phi_i}{\partial x}\right) + \frac{\mathrm{d}}{\mathrm{d}y}\left(\frac{\partial \phi_i}{\partial y}\right) + \frac{\mathrm{d}}{\mathrm{d}z}\left(\frac{\partial \phi_i}{\partial z}\right) \right\} \tag{74}$$

$$= \frac{\partial g}{\partial \phi_i} - \alpha_i \left(\frac{\partial^2 \phi_i}{\partial x^2} + \frac{\partial^2 \phi_i}{\partial y^2} + \frac{\partial^2 \phi_i}{\partial z^2} \right) \tag{75}$$

$$= \frac{\partial g}{\partial \phi_i} - \alpha_i \nabla^2 \phi_i \tag{76}$$

Substituting

$$g = \sum_i A_i \phi_i^2 (1-\phi_i)^2 + \sum_i B_i \phi_i^2 + \sum_i \left(\sum_i \frac{\beta_{ij}}{4} \phi_i^2 \phi_j^2 \right) + \frac{\gamma}{2} \phi_1^2 \phi_2^2 \phi_3^2 \tag{77}$$

into Eq. (76), the following equation is derived.

$$\frac{\delta F}{\delta \phi_i} = A_i \left(2\phi_i - 6\phi_i^2 + 44\phi_i^3 \right) + 2B_i \phi_i + \beta_{ij} \phi_j^2 \phi_i + \gamma \phi_j^2 \phi_k^2 \phi_i - \alpha_i \nabla^2 \phi_i \tag{78}$$

Appendix 2

Phase-field model simulation is carried out based on finite differential method. The microstructures of anode is made by voxel mesh, and the grids correspond to the voxels. Discretizing

$$\left(\frac{\delta F}{\delta \phi_i}\right)^{l,m,n} = A_i \left(2\phi_i^{l,m,n} - 6\left(\phi_i^{l,m,n}\right)^2 + 4\left(\phi_i^{l,m,n}\right)^3 \right) + 2B_i \phi_j^{l,m,n} + \beta_{ij} \left(\phi_j^{l,m,n}\right)^2 \left(\phi_k^{l,m,n}\right)^2 \phi_i - \alpha_i \nabla^2 \phi_i^{l,m,n} - \alpha_i \left(\frac{\phi_i^{l+1,m,n} + \phi_i^{l-1,m,n} + \phi_i^{l,m+1,n} + \phi_i^{l,m-1,n} + \phi_i^{l,m,n+1} + \phi_i^{l,m,n-1}}{(\Delta x)^2} \right) \tag{79}$$

$$\left(\frac{\partial \phi_i}{\partial t}\right)^{l,m,n} = M_i^{l,m,n} \left[\frac{D^{l,m,n}}{(\nabla x)^2} \left\{ \left(\frac{\delta F}{\delta \phi_i}\right)^{l-1,m,n} + \left(\frac{\delta F}{\delta \phi_i}\right)^{l+1,m,n} + \left(\frac{\delta F}{\delta \phi_i}\right)^{l,m-1,n} + \left(\frac{\delta F}{\delta \phi_i}\right)^{l,m+1,n} + \left(\frac{\delta F}{\delta \phi_i}\right)^{l,m,n-1} + \left(\frac{\delta F}{\delta \phi_i}\right)^{l,m,n+1} - 6\left(\frac{\delta F}{\delta \phi_i}\right)^{l,m,n} \right\} + \frac{1}{4\Delta x} \left\{ \left(\left(\frac{\delta F}{\delta \phi_i}\right)^{l+1,m,n} - \left(\frac{\delta F}{\delta \phi_i}\right)^{l-1,m,n} \right) \left(D^{l+1,m,n} - D^{l-1,m,n} \right) + \left(\left(\frac{\delta F}{\delta \phi_i}\right)^{l,m+1,n} - \left(\frac{\delta F}{\delta \phi_i}\right)^{l,m-1,n} \right) \left(D^{l,m+1,n} - D^{l,m-1,n} \right) + \left(\left(\frac{\delta F}{\delta \phi_i}\right)^{l,m,n+1} + \left(\frac{\delta F}{\delta \phi_i}\right)^{l,m,n-1} \right) \left(D^{l,m,n+1} - D^{l,m,n-1} \right) \right\} \right] \tag{80}$$

Discritizing the time with forward differential method, the phase-field simulation is conducted with (79).

References

1. Huang K, Goodenough J (2009) Solid oxide fuel cell technology: principles, performance and operations. Woodhead Publishing, Cambridge

2. Haile S (2003) Fuel cell materials and components. Acta Mater 51:5981
3. Haering C, Roosen A, Schichl H (2005) Degradation of the electrical conductivity in stabilised zirconia systems Part I: yttria-stabilised zirconia. Solid State Ion 176:253
4. Haering C, Roosen A, Schichl H, Schnfller M (2005) Degradation of the electrical conductivity in stabilised zirconia systems Part II: scandia-stabilised zirconia. Solid State Ion 176:261
5. Marina O, Canfield N, Stevenson J (2002) Thermal, electrical, and electrocatalytical properties of lanthanum-doped strontium titanate. Solid State Ion 149:21
6. Tai LW, Nasrallah M, Anderson H, Sparlin D, Sehlin S (1995) Structure and electrical properties of La1-xSrxCo1-yFeyO3. II: the system La1-xSrxFe0. Solid State Ion 76:273
7. Ullmann H, Trofimenko N, Tietz F, Stover D (2000) Correlation between thermal expansion and oxide ion transport in mixed conducting perovskite-type oxides for SOFC cathodes. Solid State Ion 138:79
8. Atkinson A, Ramos T (2000) Chemically-induced stresses in ceramic oxygen ion-conducting membranes. Solid State Ion 129:259
9. Terada K, Kawada T, Sato K, Iguchi F, Yashiro K, Amezawa K, Kubo M, Yugami H, Hashida T, Mizusaki J, Watanabe H, Sasagawa T, Aoyagi H (2011) Multiscale simulation of electro-chemo-mechanical coupling behavior of PEN Structure under SOFC operation. ECS Trans 35:923
10. Nayar A (1997) The metal databook. McGraw-Hill, New York
11. O'Hayre R, Cha SW, Colella W, Prinz F (2009) Fuel cell fundamentals. Wiley, New York
12. Kawada T, Yokokawa H (1990) Characteristics of slurry-coated nickel zirconia cermet anodes for solid oxide fuel cells. J Electrochem Soc 137:3042
13. Grew K, Chiu W (2012) A review of modeling and simulation techniques across the length scales for the solid oxide fuel cell. J Power Sources 199:1
14. Khaleel M, Lina Z, Singh P, Surdoval W, Collin D (2004) A finite element analysis modeling tool for solid oxide fuel cell development: coupled electrochemistry, thermal and flow analysis in MARC. J Power Sources 130:136
15. Lin CK, Chen TT, Chyou YP, Chiang LK (2007) Thermal stress analysis of a planar SOFC stack. J Power Sources 164:238
16. Lin CK, Huang LH, Chiang LK, Chyou YP (2009) Thermal stress analysis of planar solid oxide fuel cell stacks: effects of sealing design. J Power Sources 192:515
17. Nakajo A, Wuillemin Z, herle JV, Favrat D (2009) Simulation of thermal stresses in anode-supported solid oxide fuel cell stacks. Part I: probability of failure of the cells. J Power Sources 193:203
18. Ferguson J, Fiard J, Herbin R (1996) Three-dimensional numerical simulation for various geometries of solid oxide fuel cells. J Power Sources 58:109
19. Hall D, Colclaser R (1999) Transient modeling and simulation of a tubular solid oxide fuel cell. IEEE Trans Energy Convers 14:749
20. Yakabe H, Ogiwara T, Hishinuma M, Yasuda I (2001) 3D model calculation for planer SOFC. J Power Sources 102:144
21. Atkinson A (1997) Chemically-induced stresses in gadolinium-doped ceria solid oxide fuel cell electrolytes. Solid State Ion 95:249
22. Atkinson A, Sun B (2007) Residual stress and thermal cycling of planar solid oxide fuel cells. Solid State Ion 23:1135
23. Liu L, Kim GY, Chandra A (2010) Modeling of thermal stresses and lifetime prediction of planar solid oxide fuel cell under thermal cycling conditions. J Power Sources 195:2310
24. Chen HY, Yua HC, Cronin J, Wilson J, Barnett S, Thornton K (2011) Simulation of coarsening in three-phase solid oxide fuel cell anodes. J Power Sources 196:1333
25. Jiao Z, Shikazono N (2013) Simulation of solid oxide fuel cell anode microstructure evolution using phase field method. J Electrochem Soc 160:F709
26. Li Q, Liang L, Gerdes K, Chen LQ (2012) Phase-field modeling of three-phase electrode microstructures in solid oxide fuel cells. Appl Phys Lett 101:033909
27. Liu L, Gao F, Hu G, Liu J (2012) Phase field simulation for the evolution of textured ceramics microstructure. Ceram Int 38:5425
28. Moshtaghioun B, Garcia D, Hernandez F, Rodriguez A (2014) A phase-field model of 2D grain size distribution in ceramics. J Eur Ceram Soc 34:2731
29. Zhang Y, Xia C, Ni M (2012) Simulation of sintering kinetics and microstructure evolution of composite solid oxide fuel cells electrodes. Int J Hydrog Energy 37:3392
30. Chan S, Khor K, Xia Z (2001) A complete polarization model of a solid oxide fuel cell and its sensitivity to the change of cell component thickness. J Power Sources 93:130
31. Sanchez-Palencia E (1980) Non-homogeneous media and vibration theory. No. 127 in Lecture Notes in physics. Springer, Berlin
32. Suquet P (1987) In: Sanchez-Palencia E, Zaoui A (eds.) Homogenization techniques for composite media. Lecture Note on physics, vol 272. Springer, pp 193–278
33. Terada K, Kurumatani M, Ushida T, Kikuchi N (2010) A method of two-scale thermo-mechanical analysis for porous solids with micro-scale heat transfer. Comput Mech 146:269
34. Terada K, Kato J, Hirayama N, Inugai T, Yamamoto K (2013) A method of two-scale analysis with micro-macro decoupling scheme: application to hyperelastic composite materials. Comput Mech 52(5):1199
35. Terada K, Hirayama N, Yamamoto K, Kato J, Kyoya T, Matsubara S, Arakawa Y, Ueno Y, Miyanaga N (2014) Applicability of micro-macro decoupling scheme to two-scale analysis of fiber-reinforced plastics. Adv Compos Mater 23(5–6):421
36. Asp K, Agren J (2006) Phase-field simulation of sintering and related phenomena—a vacancy diffusion approach. Acta Mater 54:1241
37. Wang Y (2006) Computer modeling and simulation of solid-state sintering: a phase field approach. Acta Mater 54:953
38. Yasuda I, Hikita T (1993) Electrical conductivity and defect structure of calcium-doped lanthanum chromites. J Electrochem Soc 140(6):1699
39. Fukuda Y, Hashimoto S, Sato K, Yashiro K, Mizusaki J (2009) High temperature defect equilibrium, solid state properties and crystal structure of La0.6Sr0.4Co1-yFeyO3-δ($y = 0.2, 0.4, 0.6, 0.8$) for cathode of solid oxide fuel cells. ECS Trans 25:2375
40. Park J, Blumenthal R (1989) Electronic transport in 8 mole percent Y2O3-ZrO2. J Electrochem Soc 136:2867
41. Yasuda I, Hishinuma M (1996) Electrochemical properties of doped lanthanum chromites as interconnectors for solid oxide fuel cells. J Electrochem Soc 143(5):1583
42. Sasagawa T, Takahashi K, Terada K, Kawada T (2012) Estimation of macroscopic material properties using sintering simulation of porous microstructure affected by mechanical effects (In Japanese). Trans JSCES 2012:2012004
43. Emmerich H (2009) The diffuse interface approach in materials science. Springer, Berlin
44. Provatas N, Elder K (2010) Phase-field methods in materials science and engineering. Wiley-VCH, Weinheim
45. Koyama M, Ogiya K, Hattori T, Fukunaga H, Suzuki A, Sahnoun R, Tsuboi H, Hatakeyama N, Endou A, Takaba H, Kubo M, Carpio CD, Miyamoto A (2008) Development of three-dimensional porous structure simulator POCO2 for simulations of irregular porous materials. J Comput Chem Jpn 7:55

46. Baniassadi M, Garmestani H, Li D, Ahzi S, Khaleel M, Sun X (2011) Three-phase solid oxide fuel cell anode microstructure realization using two-point correlation functions. Acta Mater 59:30
47. Wilson J, Duong A, Gameiro M, Chen KTH-Y, Mumm D, Barnett S (2009) Quantitative three-dimensional microstructure of a solid oxide fuel cell cathode. Electrochem Commun 11:1052
48. Yu J, Park G, Lee S, Woo S (2007) Microstructural effects on the electrical and mechanical properties of Ni-YSZ cermet for SOFC anode. J Power Sources 163:926
49. Tietz F (1999) Thermal expansion of SOFC materials. Ionics 5:129
50. Tai LW, Nasrallah M, Anderson H, Sparlin D, Sehlin S (1995) Structure and electrical properties of La1-xSrxCo1-yFeyO3. I: the system La0. 8Sr0. 2Co1-yFeyO3. Solid State Ion 76:259
51. Fergus J (2004) Lanthanum chromite-based materials for solid oxide fuel cell interconnects. Ionics 171:1
52. Yasuda I, Hishinuma M (2000) Lattice expansion of acceptor-doped lanthanum chromites under high-temperature reducing atmospheres (in Japanese). Electrochem 68:526
53. Steinbach I, Pezzolla F, Nestler B, Sedklberg M, Ptieler R, Rezende J (1996) A phase field concept for multiphase systems. Phys D 94:135